Demonstration of 2 × 2 heterodyne receiver array at 1.4THz using HEB mixers and Fourier phase grating LO

Author: Xuxiang Liu
Supervisor: Dr. Darren Hayton, SRON
Dr. Akira Endo, TU Delft

Demonstration of 2 x 2 heterodyne receiver array at 1.4THz using HEB mixers and Fourier phase grating LO

by

Xuxiang Liu

in partial fulfillment of the requirement for the degree of

Master of Science
in Electrical Engineering

at Delft University of Technology, Netherlands Institute for Space Research (SRON).
to be defended publicly on Friday July 3, 2015 at 14:00 PM.

Group:	Terahertz Sensing Group, Department of Microelectronics
Supervisor:	Dr. Darren Hayton, SRON
	Dr. Akira Endo, TU Delft
Thesis committee:	Prof. Dr. Andrea Neto, TU Delft
	Dr. Akira Endo, TU Delft
	Dr. Darren Hayton, SRON
	Dr. Jianrong Gao, SRON/TU Delft

This thesis is confidential and cannot be made public until July 3, 2015

TU Delft

Preface

This master thesis demonstrates the realization of a 2×2 heterodyne receiver array at 1.4 THz based on superconducting hot electron bolometer (HEB) mixers and a Fourier phase grating local oscillator (LO). This is the first time to build a heterodyne receiver array based on these two techniques at such a high frequency.

The theoretical knowledge of two key components in this receiver array, HEB mixer and Fourier phase grating, have been elaborated in this thesis. The Fourier phase grating is further used in designing LO optical path to fit the array configuration. We also characterize the overall performances of this receiver array, including the required optimal pumped LO power, noise temperature, IF bandwidth and stability.

Due to the feasibility of measuring two HEB currents simultaneously in an array and the LO beam duplication property of the phase grating, we prove that the instability of the HEB current is mainly from the fluctuations in LO power, instead of the HEB mixer itself. Based on this fact, we raise an idea of stabilizing two currents using one stabilization circuit for the first time. This can reduce the complexity in designing a large array. This new stabilization method is then verified by characterizing the Allan variance time (stability) improvement comparing to non stabilization circuit applied receiver array.

This 1.4 THz receiver array can also be served as a prototype for developing future 4.7 THz array in GUSSTO project, which is proposed to flight by NASA. The performance of the 4.7 THz phase grating is characterized in this thesis as well.

This MSc thesis work is performed in Netherlands Institute for Space Research (SRON), Groningen. Meanwhile, it is also supported by Terahertz Sensing group at EWI, TU Delft. A scientific paper is written during the thesis work and published on 26th International Symposium on Space Terahertz Technology, Cambridge. The paper is attached in the Appendix.

Xuxiang Liu
16/06/2015, Groningen

Content

I

Introduction

1.1 Terahertz Astronomy

Terahertz ($\sim 10^{12}$ Hz), also known as the sub-millimeter and far-infrared radiation, is defined as a frequency range 0.3 THz to 10 THz, or from wavelength 30um to 1mm according to the ITU standard. This frequency range is perhaps the last largely-unexplored region for astronomy observation, which is partially due to the difficulty in constructing THz sources and detectors, and partially due to the radiation absorption of Earth atmosphere [1]. Thanks to the fast development of superconducting and quantum technology, lots of different THz detectors have been developed and improved, which enable people to observe the THz radiation in space.

The existed terahertz spectral lines of ions, atoms and molecules that permeate our universe hide lots of information on star and planet formation, the evolution of the galaxies, the chemistry components of interstellar clouds and etc. Furthermore, the continuum emission of star forming regions, pre-planetary disks and entire galaxies also peak at terahertz frequencies due to reprocessing of visible and ultraviolet light by dust in interstellar clouds. These spectroscopic signatures together with the bright continuum emission, lead to a rich spectrum of emission and absorption lines, which will help us to characterize and study lots of astrophysical phenomena [1].

1) Cometary Atmospheres: comets maintain lots of information about the physical and chemistry conditions of our early Solar system, since they have spent most their time in cold outer reaches of Solar system, and have not undergone thermal processing. However, it is always impossible for us to directly analyze the comet material. So the spectral line emissions like CO and CH_4 are the most powerful techniques to study the atmosphere of the comets, and its relation to the Solar System. These lines have been observed directly using heterodyne techniques by the Sub-millimeter Wave Astronomical Satellite (SWAS), and HIFI instrument on the Herschel Observatory [1].

2) Life cycle of Interstellar Medium (ISM): Figure 1 illustrates the life cycle of the interstellar clouds. This cycle is the driving force for the evolution of galaxies. For example, stars are born in the interstellar medium, and they eventually become part of that after their death. The study of this will be of great benefit to our understanding of galactic evolution. However, the molecular interstellar clouds are mainly comprised of molecular hydrogen and atomic helium, which have no accessible emission line spectra. So the tracers for probing these clouds are the rare elements, for example, the carbon. As depicted in the Figure 1, there are three states of carbon: atomic carbon (CI), carbon monoxide (CO) and ionized carbon (CII), which form a "carbon cycle". Just as the "carbon cycle" on the Earth, there is an equivalent life cycle of matter in the Galaxy which can be traced by the "carbon cycle" in the universe [1]. All of these three carbon states have been observed in the terahertz frequency region, for example, the 1.9 THz line of CII is taken by

an Herschel heterodyne detector.

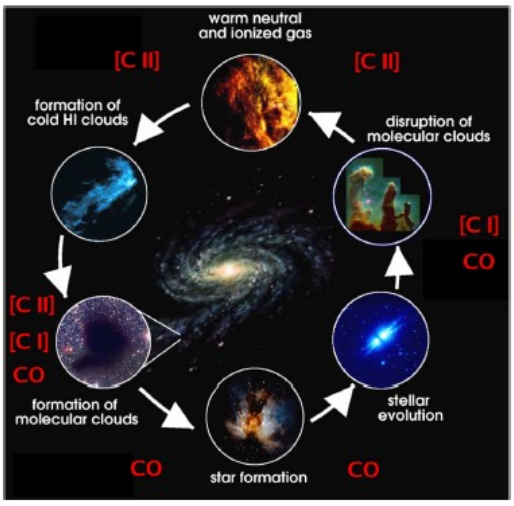

Figure 1. Illustration of various stages in the life cycle of interstellar medium. Figure from [1].

3) Nearby Galaxies: the studies of nearby galaxies always help us to understand more about the star formation in our own galaxy These studies include the structure of star forming giant molecular clouds, the inventory of star forming gas, and the heating/cooling procedures of the ISM [1], etc. The first terahertz spectroscopic measurement of external galaxies was implemented by the Kuiper Airborne Observatory. It discovered that while the 1.9 THz CII line dominates the total line cooling, the 4.7 THz oxygen line takes over the primary coolant for warmest and highest luminosity sources. The combination of the instruments SPIRE and PACS on the Herschel Space Observatory also help in studying external galaxies in terahertz frequencies.

There are more astrophysical phenomena that are relating to terahertz radiation in space, for example the planetary atmospheres, the astrochemistry of star forming region and etc. The discovery and study of these phenomenon all rely on the ground-based or space-based terahertz detection instruments. Much of this thesis will be devoted to the development of a new THz receiver array which can work at above 1THz region, and is faster and more efficient than a single pixel system.

1.2 Direct and Coherent detection

Generally speaking, the detection technology can be divided into two categories: direct detection and coherent (heterodyne) detection. Both technologies are used in terahertz detection application. Transition Edge Sensor (TES) and Kinetic Inductance Detector (KID) belong to the direct detection, while the Superconductor-Insulator-Superconductor (SIS) mixer and Hot Electron Bolometer (HEB) mixer belong to the heterodyne detection.

1.2.1 Direct detection technology

The direct detection scheme is shown in Figure 2. It works simply as a square-law detector ($P \propto V^2$, where P is the power and V is the voltage), which only preserve power amplitude information.

Since the direct detector itself has no intrinsic frequency resolving power, all frequency components which are coupled to the detector will be detected and produce a response. Thus, a band-pass filter is used before the detector to select the spectral lines we would like observe. Since the output of the direct detector is the amplitude of the power, which is a low-frequency signal, a low-pass filter is used to rule out the high-frequency noise and enhance the signal-to-noise ratio.

Ideally, this type of detector is not quantum limited, which enables the detection of arbitrary low signal level. However, background noise and detector noise will always limit the detector performance in practice [2].

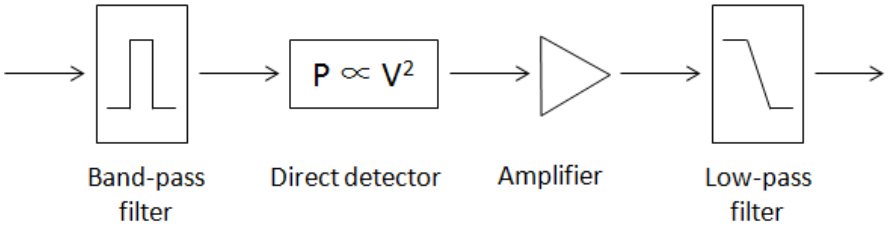

Figure 2. a simple model for illustrating the direct detection scheme. Figure from [2]

1.2.2 Coherent detection technology

The coherent detection is a technology that is based on a frequency mixer and lab-generated local oscillator signal, which is also known as the heterodyne detection. The coherent detection scheme is shown in Figure 3. In contrast to direct detection, both amplitude and phase information are preserved in coherent detection.

The local oscillator signal ($V_{LO}\sin(w_{LO}t)$) is a continuous wave with extremely stable frequency or phase, while the signal we are going to detect is ($V_{sig}\sin(w_{sig}t)$). The mixer is usually a non-linear component, for example, $I_{out} \propto V_{in}^2$. So the output of the mixer is:

$$
\begin{aligned}
I_{IF} &\propto \left(V_{LO}\sin(w_{LO}t+\varphi_{LO}) + V_{sig}\sin(w_{sig}t+\varphi_{sig})\right)^2 \\
&= V_{LO}^2\sin^2(w_{LO}t+\varphi_{LO}) \\
&\quad + V_{sig}^2\sin^2(w_{sig}t+\varphi_{sig}) + 2V_{LO}\sin(w_{LO}t+\varphi_{LO})\,V_{sig}\sin(w_{sig}t+\varphi_{sig}) \\
&= V_{LO}^2\sin^2(w_{LO}t+\varphi_{LO}) + V_{sig}^2\sin^2(w_{sig}t+\varphi_{sig}) + V_{LO}V_{sig}[\sin((w_{LO}+w_{sig})t+\varphi_{LO}+ \\
&\quad \varphi_{sig}) + \sin(|w_{LO}-w_{sig}|t+\varphi_{LO}-\varphi_{sig})]
\end{aligned}
\tag{1}
$$

Since the LO frequency w_{LO} and signal frequency w_{sig} are much faster than the device response time, the device can only detect the beat frequency signal. So the output signal is an intermediate frequency (IF) signal with a frequency of $|w_{LO}-w_{sig}|$. A spectrum analyzer is applied to retrieve the IF signal information.

Since both amplitude and phase information are preserved, as indicated by Eq. (1), the heterodyne detector is a quantum limited detector [2]. In addition, the heterodyne detector can not only detect the signal with a frequency equals to w_{sig}, but also the signal with a frequency equals to $2w_{LO}-w_{sig}$. This is known as imaging frequency signal.

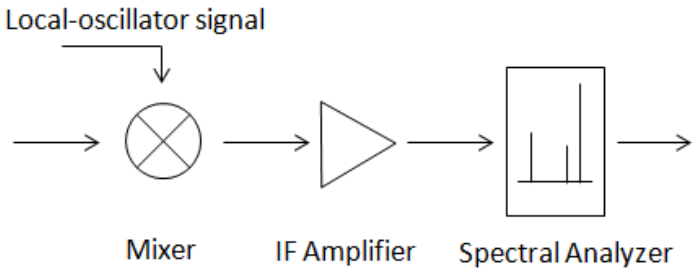

Figure 3. a simple model for illustrating the coherent detection scheme. Figure from [2]

1.2.3 Transition Edge Sensor

Transition Edge Sensor (TES) is one of the most sensitive direct detectors in sub-millimeter and infrared radiation range. The key component is a superconducting film that works close to its critical temperature (T_c). In this region, a very small change in the temperature will cause a huge change in electrical resistance, and thus we could detect the signal based on its temperature changes. Figure 4a illustrates the temperature dependent resistance of the superconducting film.

For the TES device, the T_c of the superconducting film is typically in the order of a milli-Kelvin, since lower T_c material has much better sensitivity than higher one [3]. This is different from the superconducting film used in hot electron bolometer (HEB), where a high T_c superconducting film is always preferred.

The resistance change can be detected by its current or voltage. In contrast with traditional conventional bolometers which are biased at a constant current, the TES is biased at a constant voltage and read out through the current change. This idea is raised by Irwin [4], based on the fact that the temperature of the TES needs to be maintained in its transition region which is very narrow in temperature. If the TES was biased at a constant current, then the electrical power $P_b = I^2R$ increased with temperature due to the increase of resistance near T_c. A positive electro-thermal feedback will be formed, which results in dramatic temperature change. If the TES was biased at a constant voltage, then the bias power P_b decreased with temperature due to the decrease of current I near T_c. Then it becomes a negative electro-thermal feedback that can stabilize the TES temperature.

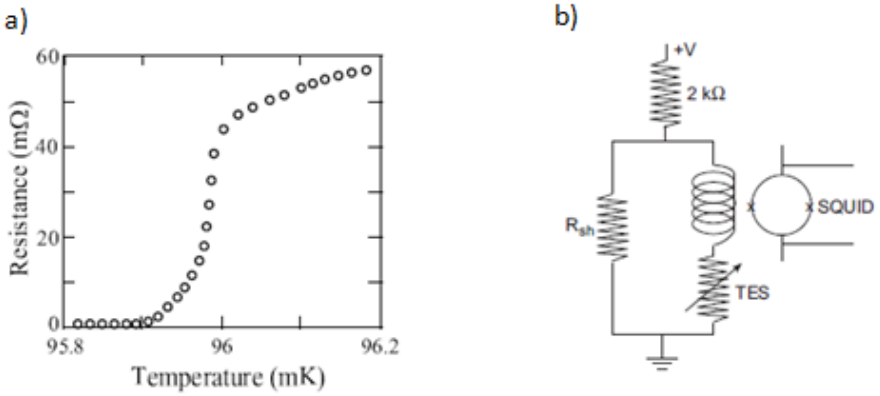

Figure 4. a: temperature versus resistance of a superconducting film used in TES; b: TES detector is coupled to the SQUIDs circuit through the coil. Current change can be detected by SQUIDs current meter. Figures from [3]

Due to the very low resistance of a TES, as shown in Figure 4a, it can only be matched to low-input impedance amplifiers, which rules out JFETS and MOSFETs [3]. Superconducting quantum interference devices (SQUIDs) are applied to read the current. The TES is coupled to the SQUID by an input coil, as depicted in the Figure 4b. The current changes in the coil will be sensed and measured by the SQUID current meter. The implementation of the SQUIDs also allows for time or frequency domain multiplexing, which is of benefit to build an array.

1.2.4 Kinetic Inductance Detector

Kinetic Inductance Detector (KID), also known as the microwave kinetic inductance detector, is another type of direct detector based on the superconducting film. It is being developed for high-sensitivity astronomical detection, also for sub-mm and far-infrared radiation.

The incident THz radiation is sensed by the superconducting film through the changes in its surface impedance. The incident radiation will create quasi-particles, which block the Cooper pairs from occupying some of the electron states. This will modify the effective pairing energy and reduce the density of pairs, and thus change the impedance [5]. This strip of superconductor is further used to make a part of a microwave resonant circuit, which can monitor the changes in the impedance through the resonant frequency change and transmitted signal phase change. Figure 5 illustrates this microwave resonant circuit and the detection principle:

In Figure 5a, the surface impedance of the KID is represented by a variable inductor part in the LC resonant circuit. This surface impedance can be described as a combination of surface inductance L_s and surface resistance R_s, $Z_s = R_s + jwL_s$. The effect of L_s is to change the inductance L, while the effect of R_s is to make the inductor slight lossy.

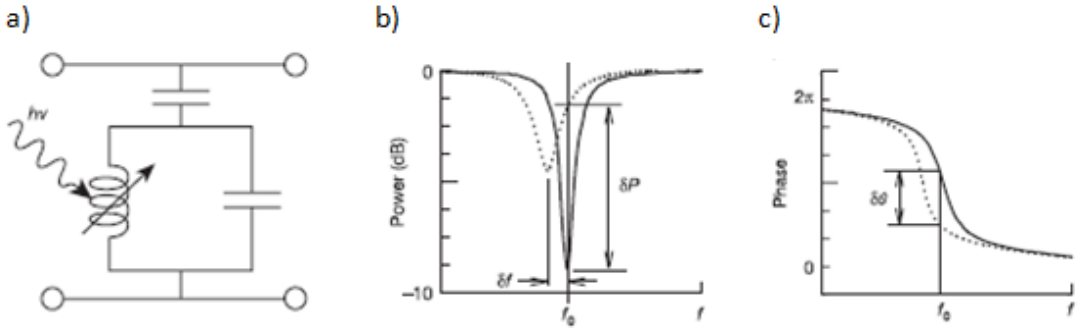

Figure 5. a: Microwave resonant circuit model, the TES is used as a variable inductor; b, c: illustration of the changes in resonant frequency, dip and signal phase due to the incoming radiation. Figures from [5]

At the beginning, the LC circuit will produce a dip at its resonant frequency in its transmission, which is determined by its original surface impedance Z_s and other constant components in the circuit. This is depicted as the solid curve in Figure 5b. When there is power illuminating on the detector, both L_s and R_s are increased which will move the resonant frequency (due to the change of L_s) and make the dip broader and shallower (due to the change of R_s) [5], as the dotted curve in Figure 5 b. This will also change the phase of the microwave signal which passes through the circuit, as shown in the Figure 5c.

1.2.5 Superconductor-Insulator-Superconductor detector

The superconductor-insulator-superconductor (SIS) detector is the most sensitive heterodyne detector in the frequency range up to roughly 1 THz. It is a device that has a "sandwich" structure: two superconductors separated by a thin insulator layer. The current passes through the insulator layer via the process of photo-assisted tunneling, which refers to a phenomenon that a particle tunnels through a barrier that it classically could not surmount. This is also the basis for SIS mixing.

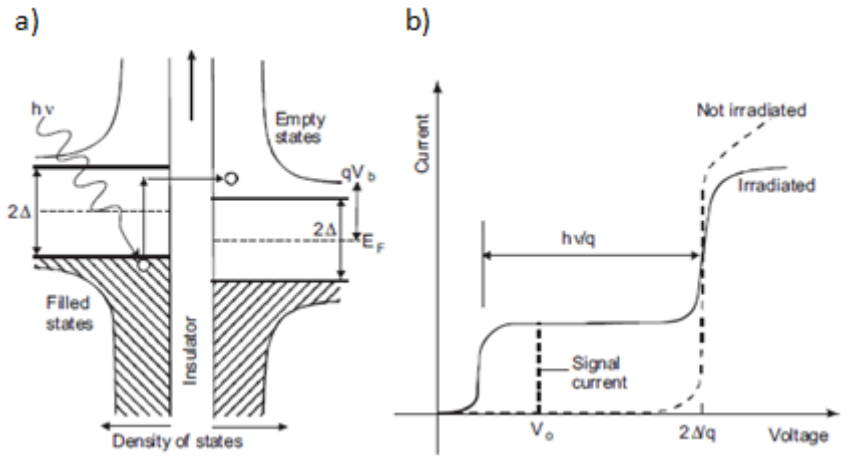

Figure 6. a: Energy gap and photon - assisted quantum tunneling illustration; b: IV curves of un-pumped and pumped SIS mixer. Figures from [6]

The operation of the SIS can be described by using the energy band representation known for semiconductors [6], as depicted in Figure 6a. The states below the energy gap (2Δ) are occupied while the state above the energy gap are empty. A bias voltage V_p, which is applied on the junction will make an energy shift qV_p between two superconductors. If the junction is also irradiated, the energy of photons hf together with the bias voltage will enable the tunneling process when $qV_b > 2\Delta - hf$. Then the electron will tunnel through and leave an un-paired quasi-particle behind.

The dotted line in Figure 6b is the an ideal un-pumped IV curve. When the bias voltage reaches the gap voltage (V_{gap}), there is a sharp rise in the current. This sharp rise in current is due to the quasi-particles tunnel from one side of the insulator to the other, where they recombine [6]. Then the strong non-linearity characteristic in the IV curve can be used for SIS frequency mixing. When there is radiation illuminated on the SIS mixer, there is already a current when the bias voltage is smaller than gap voltage ($V_p + \frac{hf}{p} \geq V_{gap}$) due to the photon-assist tunneling process. Thus, a SIS junction biased at V_p will respond to radiation in the frequency range [7]: $q(V_{gap} - V_p) < hf < q(V_{gap} + V_p)$.

In principle, the SIS mixer can approach quantum limit if the photons can be coupled efficiently to the tunnel junction. But this requires an inductive tuning circuit which can compensate for the parallel-plate capacitance of the junction. The realization of this tuning circuit becomes more difficult when the frequency becomes higher [8]. So the SIS mixer is usually used

in a frequency range not far above 1 THz.

1.2.6 Superconducting Hot Electron Bolometer Detector

Superconducting Hot Electron Bolometer (this name will be simplified as "hot electron bolometer" in the following contents) is another type of heterodyne detector which is very sensitive in the high frequency region, being an alternative to SIS mixers. The HEB consists of a thin superconducting film (bridge), which is connected with the antenna structure by the contact pads. As its name suggests, HEB mixer works on the principle of bolometric effect, which utilizes a bolometric effect on which the radiation power changes the temperature, thus the resistance [6], as shown in the Figure 7.

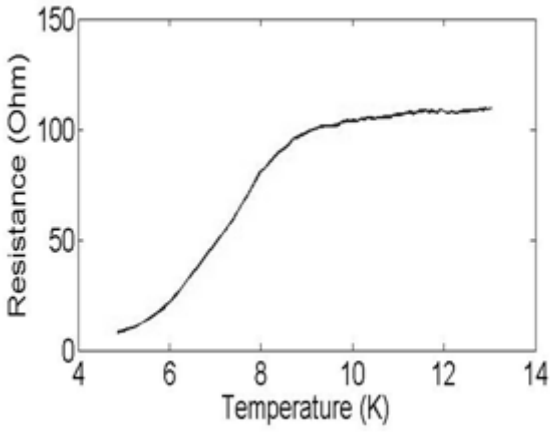

Figure 7. Temperature dependent resistance of a superconducting film, which is used as the key mechanism to realize mixing.

The incoming LO photon energy together with the bias voltage applied on the HEB mixer can heat the superconducting bridge and can increase the temperature of electrons (or quasi--particles). A so called "hot electrons" region will be created on the superconducting bridge and the resistance will also be increased [2]. When the detecting signal is coming, the photon power dissipated in the superconducting bridge is:

$$P_B(t) = \frac{[V_{LO}\cos(w_{LO}t) + V_s\cos(w_s t)]^2}{2R_0} \tag{2}$$

According to the mixer theory, the resulting intermediate frequency (IF) signal power is: $P_{IF}(t) \propto \cos(|w_{LO} - w_s|t)$. Due to the limitation of the responding time (cooling ability), only this IF signal power will be cooled down through the electron-phonon interaction (phonon cooling) or diffuse through contact pads (diffusion cooling). This also means the resistance of the film will be modulated at the IF frequency, while other frequency components in Eq. (2) will be ruled out.

As a result, we can detect this IF signal through the resistance changes, and retrieve the incident signal information. More detailed physical phenomenon and theoretical knowledge relating to phonon cooling HEB detector is referred to Chapter II.

1.3 State of the Art

1.3.1 Heterodyne Receiver Overview

THz heterodyne receivers, based on SIS mixer and HEB mixer, are generally the preferred detectors for high resolution spectroscopic studies in astronomy. Although only a handful of heterodyne array instruments at terahertz frequency with a limited number of pixels are operational (mainly are SIS mixer or waveguide-based HEB mixer within 1THz region) currently, there is an increasing demands for higher frequency (above 1THz) arrays with high resolution, high mapping speed and multiple line spectroscopy [9]. In addition, the development of the array not only helps to increase the speed, but also allows for various self-calibration scheme and study on stability of device.

The main issues relating to the array design are circuit components integration, LO power multiplexing and injection, and front-end architecture. The front-end architecture includes the mixer selection and array configuration. In all of these issues, LO multiplexing and available LO power in each pixel are the most important concerns, since they determine the front-end architecture. As a result, there are few published results from high frequency heterodyne arrays.

Table I summarizes operational or under developed heterodyne array instruments [10 ~17] :

Table I. Heterodyne Array Summary

Instrument /Platform	**Front-end**	**Frequency**	**LO multiplexing scheme**	**Efficiency (Total)**
PolarStar /ASTRO telescope	2×2 SIS mixer array (Quasi-optic)	850 GHz	Quasi-optic power divider, made from two low-loss beam splitter	~ 72%
DesertStar /Heinrich Hertz telescope	7 SIS mixer array in hexagonally shape (Quasi-optic)	345 GHz	Phase grating	~ 80%
SMART/ KOSMA telescope	2×4 SIS mixer array (Quasi-optic)	490/810 GHz	Collimating Fourier grating	-
HERA/IRA M telescope	3×3 SIS mixer array (Waveguide based)	230 GHz	3 way waveguide power splitter	-
CHAMP+/ ALMA	2×7 SIS mixer array (Quasi-optic)	690/810 GHz	Collimating Fourier grating	~ 70%
STO observatory	2×4 HEB mixer array (Waveguide based)	1.4/1.9 THz	Waveguide power splitter (under development)	-
upGreat/ SOFIA	2×7 HEB mixer array (Waveguide based)	2.5/4.7 THz	Waveguide power splitter (underdevelopment)	-
TFPA[1]	1×3 HEB mixer array (Quasi-optic)	1.6 THz	De-focused LO beam	-

Note. 1: TFPA: Terahertz Focal Plane Array, this is only a prototype published in the [17].

1.3.2 GUSSTO Project

Galactic/Xgalactic Ultra long duration balloon Spectroscopic Stratospheric THz Observatory (GUSSTO) is a project proposed to NASA to fly on a long duration balloon from the Antarctic. The Dutch research groups at SRON and TUDelft will contribute to the science of this project, and also a 4.7 THz Hot electron bolometer receiver array.

For an ideal array, the desired LO should be equally and uniformly distributed into each pixel with no losses (or very little losses). The main splitting technique includes the waveguide power splitter and quasi-optic one, as indicated in the Table I. While the waveguide techniques are available, they become very lossy and difficult to implement when the frequency goes high. A defocused beam is easy to implement in high frequency range, but it is very poor in efficiency especially when the spacing between each element is large.

In the GUSSTO project, a new Fourier phase grating is designed and manufactured to form a multi-beam LO at 4.7 THz. The use of a Fourier phase grating to split a single incoming THz source has already proved to be feasible and highly efficient in previous low frequency SIS mixer receiver arrays. However, it is the first time to implement a Fourier phase grating at such a high frequency, and to build a quasi-optic HEB receiver array based on this technique

1.4 Goal of the Thesis

In this thesis, we are going to build and demonstrate a complete 1.4 THz quasi-optic HEB receiver array based on a Fourier phase grating split LO source for the first time, which can serve as a prototype for the future 4.7 THz receiver array in GUSSTO project. The optical path, LO distribution, and receiver array will be designed, characterized and analyzed. We will investigate the feasibility of stabilizing two pixels simultaneously using only one PID controller, which allows a much simpler stabilization configuration. To the authors best knowledge, this has never been done in a previous receiver array. In addition, we will also characterize the performance of the very first 4.7 THz Fourier phase grating, which will be the crucial component in the GUSSTO project.

The thesis is organized as following: Chapter II will introduce the theory and coupling of the HEB device. The front-end configuration in our receiver will also be described. Chapter III will talk about the Fourier phase grating theory. Chapter IV will talk about the theoretical background of the receiver performances and their measurement methods. Chapter V will be the characterization of a 1.4 THz and 4.7 THz grating performance. Chapter VI will illustrate the array measurement setup and LabView controlled RF test facilities. Chapter VII will be the characterization of the whole array, including the IV curve, noise temperature, IF bandwidth and stability. Chapter VIII will be the summary and outlook.

II

Hot Electron Bolometer Mixer

2.1 Conventional Bolometer Working Principle

A bolometer is a detector for measuring the energy of incident electromagnetic radiation. The thermal model for a simple bolometer is shown in the Figure 8:

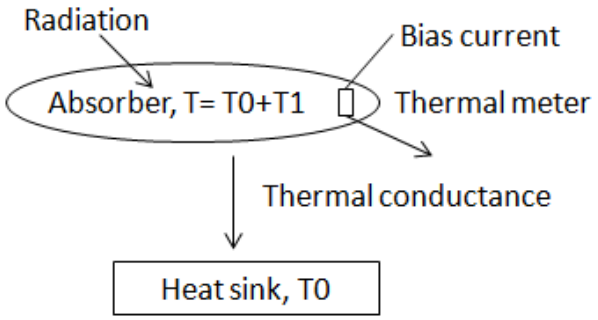

Figure 8. Conventional bolometer principle. Figures from [19].

The operation of the bolometer is as follows [18]: an absorber is firstly connected to a heat sink with a temperature T_0 through a thermal conductance G (Watts per Kelvin). Then the absorber is absorbing a constant power P_0 which raise its temperature by T_1 above the heat sink. And there is Eq. (3):

$$G = \frac{P_0}{T_1} \tag{3}$$

Now assuming that we are detecting a periodic signal, which can be regarded as adding a variable power component $P_v(f)$, and then there is Eq.(4):

$$\eta P_v(t) = C\left(\frac{dT_1}{dt}\right) \tag{4}$$

where η is the efficiency of the absorber and C is the heat capacity. So the total power $P_T(t)$ is:

$$\begin{aligned} P_T(t) &= P_0 + \eta P_v(t) \\ &= GT_1 + C\left(\frac{dT_1}{dt}\right) \end{aligned}$$

(5)

Supposing the $P_v(t)$ is a step function, and it equals to 0 when t < 0, it equals to P_1 when t > 0, then the solution to (5) is:

$$T_1(t) = \begin{cases} \frac{P_0}{G}, & t < 0 \\ \frac{P_0}{G} + \frac{\eta P_1}{G}\left(1 - e^{-t/(\frac{C}{G})}\right), & t \geq 0 \end{cases} \tag{6}$$

So when the time t is much larger than the thermal time constant C/G, the measured temperature $T_1(t)$ is proportional to $(P_0 + \eta P_1)$. Thus we can measure the input signal power.

The absorber will absorb the photons and convert their energy to heat. In this process, the wavelength is irrelevant, and the detector responds the same so long as the energy of the absorbed photons is the same. Thus, the wavelength dependence of responsibility is flat and as broad as the absorbing material could allow. By fully optimizing the absorbing material, the efficiency η can be as high as 90-100% [18]. So a bolometer based on superconducting material is a very good candidate for detecting weak signal, especially in sub-millimeter range.

2.2 Hot Electron Bolometer Principle - Hot Spot Model

A conventional bolometer usually consists of separate absorber, thermometer, thermal link and heat sink. For a hot electron bolometer, all of these elements are combined as shown in the Figure 9b. The superconducting bridge served as both the absorber and thermometer. The heat sink and thermal link, depends on cooling mechanism, are silicon substrate/contact pads and electron-phonon interaction/diffusion.

In Figure 9b, the two contact pads are bi-layers of normal metal and a thin superconducting film which is also used for micro-bridge itself. The contacts are in superconducting state since the bath temperature (T_b) is usually lower than the reduced critical temperature (T_c) of the contact pads. When a DC current is passing through the bridge and together with the irradiated LO power, a resistive region will be formed as soon as the critical current density is exceeded. The two contact pads will remain superconducting state since the current here is still very low [19].

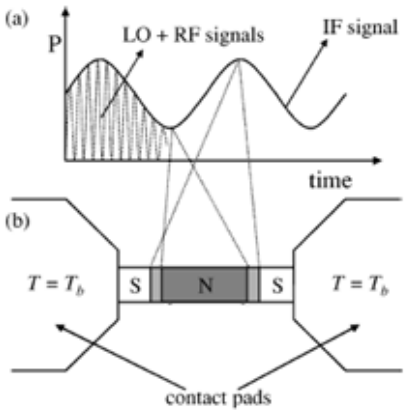

Figure 9. a: dotted line is the LO and RF power as a function of time, solid line is the beat

frequency signal (IF signal) as a function of time; b: illustration of the HEB structure. The S stands for superconductor region, and N stands for normal resistance region. The IF signal actually modulates the length of the resistance region. Figures from [19].

According to [19], the resistive behavior is dominated by the form of a "hotspot region" when the temperature is low while the current density is high. So firstly an electronic hotspot region is formed in the center of the superconducting bridge due to the heat from the combined DC and LO power. When an RF signal with a slightly different frequency is applied, it together with the LO signal, will generate a beat frequency component. This beat frequency signal will modulate the dissipated power into the superconducting bridge and thus modulate the length of the "hotspot region", as shown in the Figure 9a and 9b. As a consequence, the resistance is modulated by this beat frequency signal and enables the detection. In practice, the DC power can only be absorbed by the hot spot region, while the LO and RF signal can be uniformly absorbed by whole bridge.

In a conventional bolometer, the thermal time constant C/G determines the signal frequency we could measure, since the measured temperature is proportional to the incoming power only when the time t (1/f) is much larger than the time constant. In an HEB, the time constant for bringing the electron energy out of the superconducting bridge also determines the cut-off frequency. There are two ways to implement this cooling procedure, which are phonon-cooling and diffusion cooling. The difference between them is the process for energy relaxation. For a phonon-cooled HEB, the cooling mechanism is via the electron-phonon interaction (τ_{e-ph}, electron-phonon interaction time) and the escape of the phonon into the substrate (τ_{esc}, phonon escape to substrate time), while for diffusion-cooled HEB, the cooling is via the out diffusion of the electrons into the contact pads. This thesis will focus on the HEB mixer based on the phonon-cooling.

As depicted in the Figure 9b, the whole mixing can be explained by the change of hot spot length due to the RF, LO and DC power. So a mathematical model can be build for this HEB based on the hot spot length as a function of power [20]. This model allows non-homogenous heating to be included, which is different from the other two models that will be introduced later.

The first step for this model is to set up the hot spot region length based on the electron temperature along the superconducting bridge, which is obtained from a power balance between the local heating power (P_{LO}, P_{DC}) and the losses due to electron-phonon interaction. There is:

$$\lambda \frac{d^2}{dx^2} T(x) - \sigma[T(x) - T_b] + \left[\frac{1}{2L} P_{LO} + P_{DC} \frac{\big(U(x+H) - U(x-H)\big)}{2H}\right] = 0$$

$$T(+L) = T(-L) = T_b \tag{7}$$

where λ is the thermal conductivity of the electrons. $\sigma \propto \frac{c_e}{\tau_{e-ph}} D$ stands for the cooling efficiency, where D is the superconducting bridge cross and c_e is the heat capacity of the electron. The bridge length is L, and the hot spot region length is H. x denotes the a coordination in bridge direction and the center of this coordination is at the center of the bridge. $U(\cdot)$ function stands for

a step function, since the DC power (P_{DC}) is restricted in the hot spot region only, while the LO power (P_{LO}) is absorbed in the whole bridge. The boundary condition is that the ends of the bridge (contact pads) have the bath temperature. This is also illustrated in Figure 9.

In order to solve Eq.(7), we introduce another parameter, thermal healing length, $\mathrm{c} = \sqrt{\frac{\lambda}{\sigma}}$. This is actually the square root of the ratio between thermal conductivity and cooling efficiency. Then the solution for Eq.(7) is:

$$\mathrm{T(x)} = \mathrm{T_b} + \frac{e^{\frac{(-H-x)}{\sqrt{c}}}\left(e^{\frac{L+x}{\sqrt{c}}} - 1\right)}{2\left(1+e^{\frac{2L}{\sqrt{c}}}\right)}\left[\frac{1}{2H}P_{DC}\left(e^{\frac{2H}{\sqrt{c}}}-1\right)\left(1+e^{\frac{L+x}{\sqrt{c}}}\right)+\frac{1}{L}P_{LO}e^{\frac{H}{\sqrt{c}}}\left(e^{\frac{L}{\sqrt{c}}}-e^{\frac{x}{\sqrt{c}}}\right)\right]$$
$$+\frac{P_{DC}}{H}e^{\frac{-H-x}{\sqrt{c}}}\left[\left(e^{\frac{H}{\sqrt{c}}}-e^{\frac{x}{\sqrt{c}}}\right)^2 U(x-H)-\left(e^{\frac{H+x}{\sqrt{c}}}-1\right)^2 U(x+H)\right] \quad (8)$$

The hot spot length H for a given P_{LO} and P_{DC} can be obtained by solving Eq.(8) for:

$$\mathrm{T(H)} = \mathrm{T_c} \quad (9)$$

which indicates that the ends of the hot spot region is in the state of superconducting. This can also be referred to Figure 9b. The results for hot spot length as a function of P_{LO} and P_{DC} is plotted in the Figure 10a.

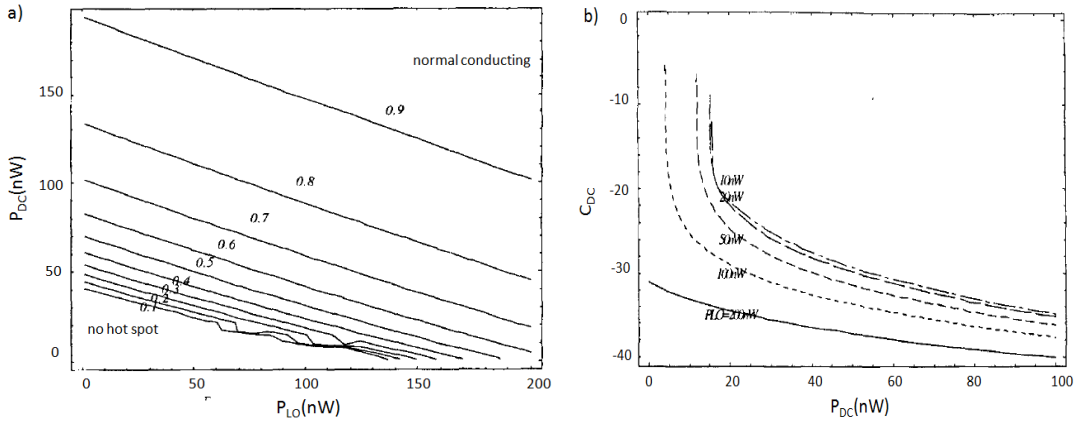

Figure 10 a: The normalized hot spot length is determined by the combination of LO power and DC power. The normalization is the ratio of the hot spot length and the bridge length. When the normalized hot spot length equals to one, it indicates that the whole bridge becomes normal resistance. When the applied power is not sufficient, there is no hot spot length; b: The self heating parameter as a function of DC power, at different P_{LO} level. Figures from [20]

As a result, the change in the hot spot length due to the change in the P_{LO} and P_{DC} can be determined by the differential of hot spot length and power change. The change of hot spot length

due to the RF power and DC power are:

$$C_{RF} = \frac{R_N}{L}\frac{\partial H}{\partial P_{LO}}$$
$$C_{DC} = \frac{R_N}{L}\frac{\partial H}{\partial P_{DC}} \tag{10}$$

The C_{DC} is also known as the "self heating". The result of C_{DC} as a function of P_{DC} at different P_{LO} value is illustrated in the Figure 10 b). When there is no hot spot region, the C_{DC} does not exist anymore. When there is a very small hot spot region, the tiny change in the P_{DC} has a significant influence in the hot spot region length. When the heating power is large, the hot spot region is less sensitive to the change in the heating power.

The second step for setting up the model is to look at the small signal model for the bolometer, where we regard it as a parametric oscillator with a load circuit, as shown in the Figure 11a.

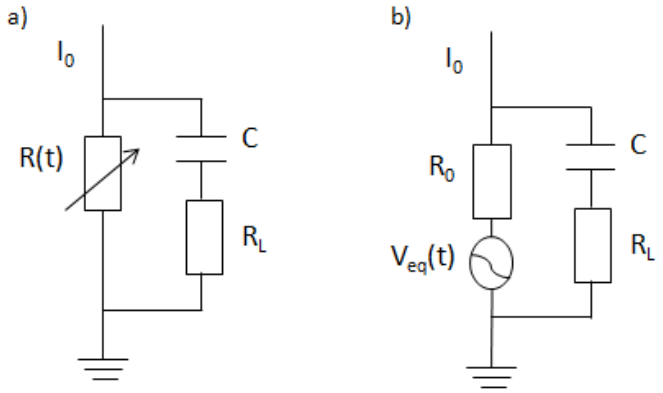

Figure 11. a: small signal model for parametric oscillator, R(t) represents the bolometer, the series of C and R_L is the load circuit, b: equivalent circuit of this parametric oscillator. Figures from [20]

The time varying resistance R(t) represents the bolometer, which is modulated by the IF signal. I_0 is the DC bias of the bolometer. The capacitor C in the load circuit is used to get rid of the DC component and the resistance R_L reads out the IF signal. The equivalent circuit for this parametric oscillator is depicted in the Figure 11b, where the R(t) is replaced with a voltage source $V_{eq}(t)$ and a bath temperature determined resistance R_0. Based on this equivalent circuit, the R(t) can be expressed as:

$$R(t) = R_0 + C_{DC}v(t)i(t) + \frac{1}{2}C_{RF}[P_{LO}P_{RF} + \sqrt{P_{LO}P_{RF}}\cos(w_{IF}t)] \tag{11}$$

where v(t) and i(t) are the time varying device voltage and current, w_{IF} is the IF signal frequency.

The v(t) and i(t) can be expressed as:

$$v(t) = V_0 + R_L i_L \cos(w_{IF} t)$$
$$i(t) = I_0 + i_L \cos(w_{IF} t) \tag{12}$$

where V_0 and I_0 are the DC voltage and current. By solving the Eq. (11)(12), we can approximate the relation between V_0 and I_0, which is also known as the DC resistance at bias point (V_0, I_0):

$$R_b = \frac{V_0}{I_0} = \frac{(C_{RF} P_{LO} + R_0)}{1 - C_{DC} I_0^2} \tag{13}$$

The last step for building this model is to obtain the IF current in the load circuit, which enables the calculation of IF gain. The IF current and gain can be calculated through the Eq. (11)(12):

$$i_L = \frac{C_{RF} I_0 P_{RF}}{R_L + R_b + C_{DC} I_0^2 (R_b - R_L)}$$
$$G = \frac{P_{IF}}{P_{RF}} = \frac{2 R_L P_{LO} P_{DC}}{R_b (R_L + R_b)^2} \left[\frac{C_{RF}}{1 - \frac{C_{DC} I_0^2 (R_L - R_b)}{R_L + R_b}} \right]^2 \tag{14}$$

Thus, a model describing the hot electron bolometer mixing principle has been setup. As we can see from Eq. (14), the generation of IF signal is due to the parametric oscillation of the bolometer resistance and a DC bias current through the device.

2.3 Other Models for Hot Electron Bolometer

Besides the hot spot model, there are other two models which were previously widely used to describe the principle of hot electron bolometer mixing: Standard Model and Nebosis-Semenov-Gousev-Renk (NSGR) model [21,22].

Unlike the hot spot model, where the DC power is absorbed only in hot spot region, the Standard Model and NSGR models are all uniform heating model which assumes the temperature is determined by the total absorbed power (DC power, sig Power and LO power) of the HEB, and is uniformly distributed along the whole superconducting bridge. So we can simply regard the HEB as a power controlled resistor.

The difference between the Standard Model and NSGR Model is the description of the energy relaxation time. In the Standard Model, we use only one single time constant τ to describe the relaxation time based on the assumption that $\tau_{e-ph} \gg \frac{c_e}{c_{ph}} \tau_{esc}$, where τ_{e-ph}, τ_{esc} and c_e are the same as in the hot spot model, while c_{ph} is the specific heat of phonon. In the NSGR

Model, however, the relaxation time is characterized by three parameters τ_1, τ_2, τ_3, which are functions of τ_{e-ph}, τ_{esc} and ratio c_e/c_{ph}.

$$\varphi(w) = \frac{(1+jw\tau_1)(1+jw\tau_2)}{1+jw\tau_3}$$

$$\tau_3^{-1} = \tau_{esc}^{-1} + \tau_{eph}^{-1}\frac{ce}{cph}$$

$$\tau_{1,2}^{-1} = \frac{\tau_3^{-1}+\tau_{eph}^{-1}}{2}\left[1 \pm \sqrt{1 - \frac{4\left(\tau_3^{-1}+\tau_{eph}^{-1}\right)^{-2}}{\tau_{esc}\tau_{eph}}}\right] \tag{15}$$

Based on the relaxation time constant, the Standard and NSGR model can predict the IF current and gain as well as the hot spot model.

2.4 Antenna, Lens and Quasi-Optical Coupling

For the quasi-optical coupled HEB, a silicon lens together with a planar antenna is the best candidate for efficiently coupling LO and RF power into the HEB. Two most widely used planar antennas are log-periodic antenna and twin-slot antenna. The silicon lens also have different shapes, like hemisphere, elliptical etc. In this thesis, all HEB pixels we use are coupled by a twin-slot antenna with an elliptical silicon (Si) lens.

2.4.1 Twin slot antenna

Figure 12 is the illustration of twin slots. The shadow region is the metal plates, while the twin slots are in the xz plane, and are along the z direction. Assuming the half space in +y direction is the dielectric substrate with ε_r. In this way, the antenna will radiated most of its power into the dielectric side. The radiation pattern can be calculated through the magnetic current distribution in the slot [23].

$$I = I_{max}\sin[k_m(l - |z|)], -l < z < l$$
$$k_m = \frac{2\pi}{\lambda_m} = \frac{2\pi\sqrt{\varepsilon_m}}{\lambda_0} \tag{16}$$

where l is half length of the slot, and $\varepsilon_m = \frac{1+\varepsilon_r}{2}$ is the average relative permittivity on the interface of air and substrate. Then the normalized field pattern in H-plane is:

$$E_{nor} \propto \frac{\sin\theta[\cos(k_e l\cos\theta) - \cos(k_m l)]}{k_m^2 - k_e^2\cos^2\theta} \tag{17}$$

where $k_e = k_{die} = \frac{2\pi}{\lambda_{die}}$ for the dielectric substrate side, while $k_e = k_{air} = \frac{2\pi}{\lambda_{air}}$ for the air side. θ is the angle from +z to +x in xz plane. The element field in E-plane is a constant, so only the array factor is considered in this plane:

$$AF \propto \cos(k_e d \sin\theta \cos\psi) \tag{18}$$

where ψ is the angle from +x to +y in xy plane, and d is the spacing between two slots. Other parameters are the same as above.

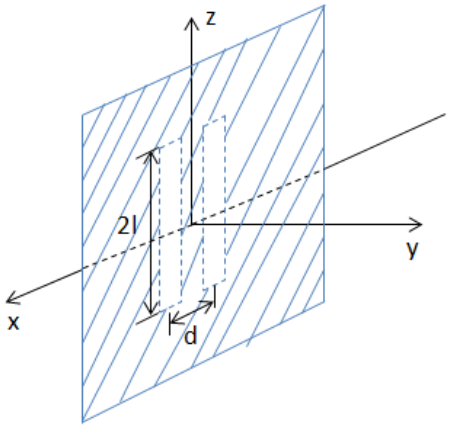

Figure 12. Illustration of twin slots. The half space in +y direction is the dielectric substrate, while in -y direction is air. The slot length is 2l, and the spacing between each slot is d.

2.4.2 Elliptical lens and AR coating

The dielectric silicon lens is used to make the beam pattern unidirectional and to increase the antenna gain. The elliptical lens is compatible to a large f-number system since it can achieve a really narrow beam and couple well to the Gaussian-beam at its minimum waist [23], also known as a good "Gaussicity" performance.

An elliptical lens is designed from an extended hemisphere lens by choosing an appropriate extension length. The extension length L is chosen to make the focus of the ellipse has the same coordination as the focus of the extended hemisphere. The principle of designing an elliptical lens is shown as below [24]:

The definition equation of a ellipse and its optical focal length (c) is:

$$\frac{(x-a)^2}{a^2} + \frac{y^2}{b^2} = 1$$

$$c = \sqrt{a^2 - b^2} \tag{19}$$

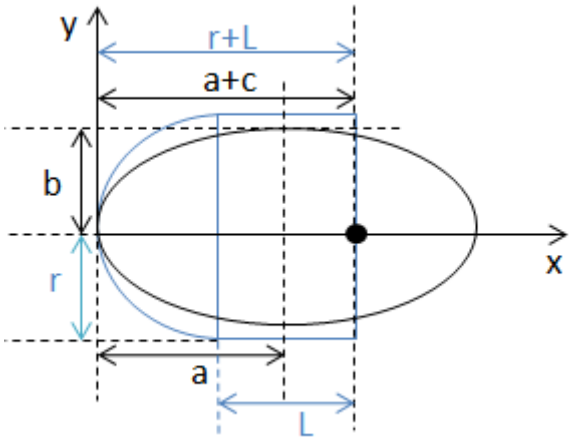

Figure 13. synthesize an elliptical lens from an extended hemisphere lens

Due to the refraction index of the dielectric ($n = \sqrt{\varepsilon_r}$), the eccentricity of the ellipse is:

$$e = \frac{\sqrt{a^2 - b^2}}{a} = \frac{1}{n} \tag{20}$$

and then there is:

$$c = \frac{a}{n} \tag{21}$$

So the coordination for the more distant focal point is $a + c$, as shown in the Figure 13. Now assuming a hemisphere with an extended length L. The equation of the hemisphere is:

$$\frac{(x - r)^2}{r^2} + \frac{y^2}{r^2} = 1 \tag{22}$$

So the distance from the tip of the hemisphere to the end of its extension length is $r + L$, and this distance should be equal to the distance from the tip of ellipse to its more distant focal point $a + c$.

As a result, the extension length L is:

$$L = a + c - r = \frac{b}{\sqrt{1 - \frac{1}{n^2}}}\left(1 + \frac{1}{n}\right) - r \tag{23}$$

For a given refraction index, the b is varied until the extended hemisphere has the closest

geometry shape as the ellipse.

Since the lens has the same dielectric property as the antenna dielectric substrate, in principle there is no reflection between each other. There will only be reflection losses from the interface between the silicon lens and air, as illustrated in Figure 14a.

One method to reduce this reflection loss is to apply an anti-reflection coating (AR coating) on the silicon lens, as shown in Figure 14b. The coating has a relative permittivity of $\varepsilon_m = \sqrt{\varepsilon_r}$ and a thickness of $d = \frac{\lambda_m}{4}$. The principle of this AR coating is that the difference in optical path between the incident and reflective wave is $\frac{\lambda_m}{2}$, which indicates that the two waves are out of phase. So they cancel with each other at the interface, and thus enhance the transmission.

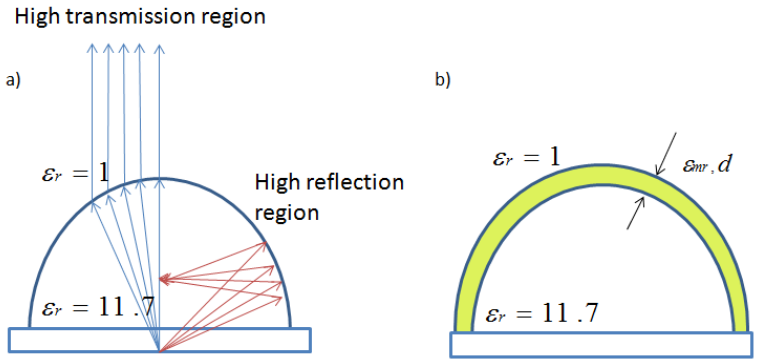

Figure 14. a: the reflection loss from the interface of silicon lens and air; b: illustration of the AR coating.

2.5 Our Choice

In this thesis, four HEB mixers we used in the array are manufactured by Dr. Nathan Vercruvssen at Kavli Institute of NanoScience at TU Delft. All of them have the same physical dimensions. The resistances of them at the room temperature are slightly different from each other, as indicated in the Table II.

Table II. Physical dimensions of four HEB mixers

	Frequency (THz)	**W bridge (um)**	**L bridge (um)**	**Thickness (nm)**	**R_{rt} (Ohm)**
NV 06 10A	1.4	1.5	0.19	7	111.1
NV 06 10b					108.0
NV 06 10C					111.6
NV 06 6b					106.7

As mentioned before, the RF and LO power are coupled to the HEB mixer using a twin slot antenna with a Si elliptical lens, which operates at 1.4 THz. The illustration of the physical dimensions of the antenna and the photo obtained from Olympus microscope are shown in the Figure 15a and b.

The length, width of the slot, and the spacing between each slot are designed according to the following rules: $2l = 0.28\lambda_{air}, w = 0.023\lambda_{air}$ and $d = 0.16\lambda_{air}$. After the antenna structure, a

RF choke filter is applied to avoid the leakage of RF signal from the IF output line [25].

The drawing of the elliptical lens is shown in the Figure 16, and the equation for this lens shape is:

$$\left(\frac{x}{a}\right)^2 + \left(\frac{y}{b}\right)^2 = 1$$
$$a = 5, b = 5.228 \tag{24}$$

In order to reduce the reflection losses, we also add an AR coating for this elliptical lens, which has a thickness of 27um. This thickness corresponds to a middle frequency between 1.4 ~ 1.9 THz (thickness for 1.4 THz is 31.5um, for 1.9 THz is 23.2um), since this coating will be used for both 1.4 and 1.9 THz HEB mixer in the STO2 project, which will fly in the end of 2015. And we will prove that this coating indeed works in the Chapter VII.

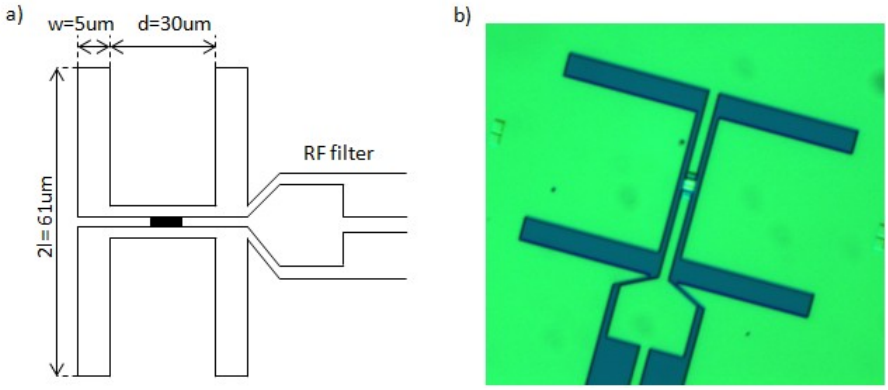

Figure 15. a: illustration of the twin slot antenna used in this thesis, which works at 1.4 THz; b: twin slot antenna photo, taken under the Olympus microscope.

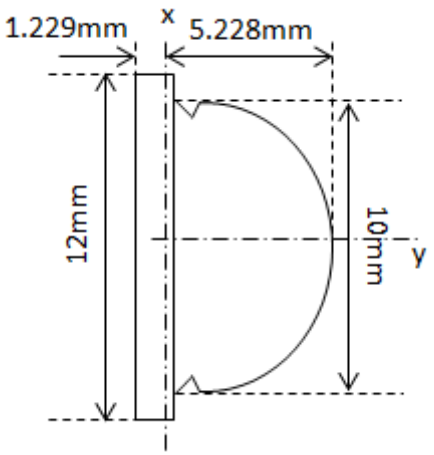

Figure 16. Physical dimensions of the Si elliptical lens used in this thesis

The normalized beam pattern of this twin slot antenna together with this lens (no coating) is simulated by the software package PILRAP [26], and is plotted in the Figure 17. The result

indicates a very narrow and highly directional beam.

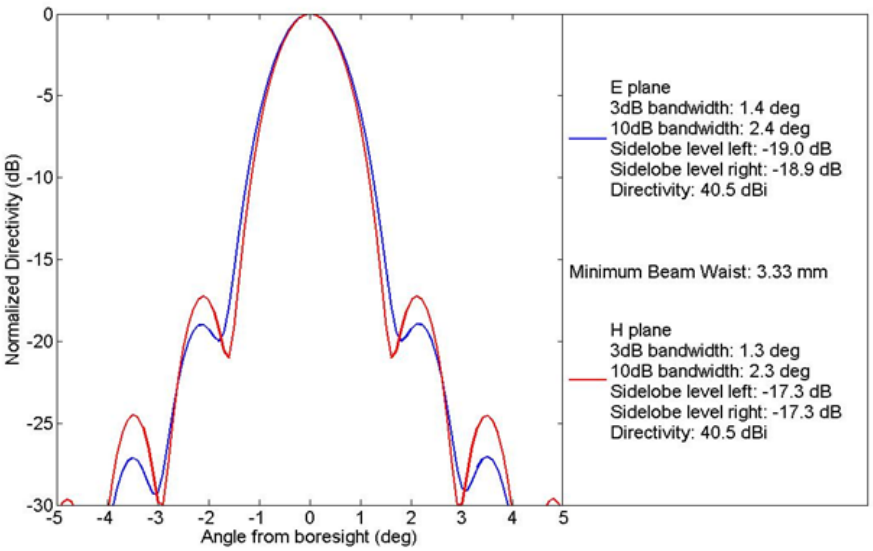

Figure 17. Normalized beam pattern of the twin slot antenna with lens at 1.4 THz. The beam is very narrow in both E and H plane, with a 3dB bandwidth of ~1.4 deg. The directivity can achieve ~40.5dB in both planes.

Four HEB pixels are arranged in a 2×2 array with a spacing of 12mm between each element, as shown in Figure 18a. The diameter of each hole is 10mm, which fits the diameter of the lens. The large spacing and narrow beam pattern ensure that there is negligible cross talk between each element in this array. The order of each HEB mixer is indicated in the Figure 18b.

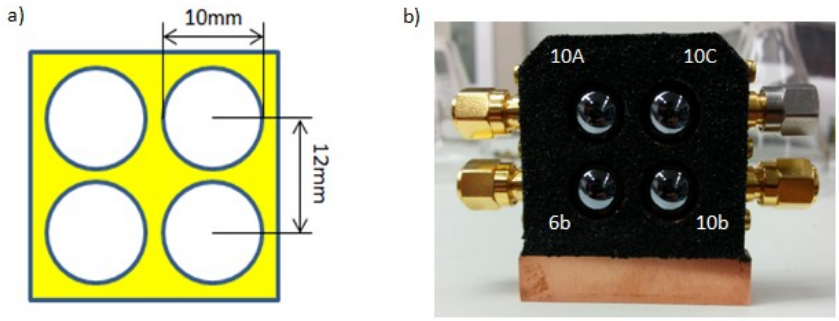

Figure 18. a: illustration of the mixer block; b: photo of the mixer block with 4 HEB pixels, absorbing material (black parts) and short terminals.

In order to reduce the reflections from the metal surface of the mixer block, which may influence the incident LO beam pattern, we put black absorbing material on the surface.

III

Fourier Phase Grating

3.1 Fourier Phase Grating Theory

The grating is an optical component with periodic strictures on its surface, which can equally split one incident beam into several sub-beams. The direction of these sub-beams are determined by the incident beam wavelength and spacing between the grating unit. A phase grating is a kind of grating, which splits the beam by modulating the phase of the incoming beam.

An easy way to understand the principle of the phase grating is to start with the path difference between two adjacent beams, which determines the constructive/destructive interference. The grating can be viewed as an array of narrow slits. The constructive and destructive interference between each slit will generate the sub-beam pattern., as shown in the Figure 19.

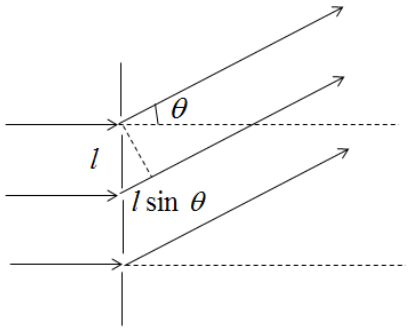

Figure 19. illustration of optical path difference. The spacing between two slits is l, the emergent angle is θ, and the path difference is lsin(θ)

If we look from the far-field, the path difference between any two diffracted beams is:

$$\Delta l = l\sin(\theta) \tag{25}$$

which is also known as the grating equation. The path difference Δd determines whether the interference is constructive or destructive:

$$l\sin(\theta) = \begin{cases} n\lambda, & \text{constructive interfernece} \\ \left(n + \frac{1}{2}\right)\lambda, & \text{destructive interference} \end{cases}$$

(26)

where n determines the order (or mode) of diffraction. The path difference, on the other hand, is actually another form of phase difference. When the two waves have constructive interference the phase difference $\Delta\varphi$ is always $2n\pi$, $(n = 0,1,\dots)$, while when two waves have destructive interference the $\Delta\varphi$ is always $(2n+1)\pi$, $(n = 0,1,\dots)$. As a result, the phase difference, instead of the path difference, becomes a key factor in determining the interference type. The relation between the phase difference and path difference is:

$$\Delta l = \frac{\lambda\Delta\varphi}{2\pi} \tag{27}$$

For a reflective grating, the optical path will be doubled. So the Eq.(27) becomes:

$$\Delta l = \frac{\lambda\Delta\varphi}{4\pi} \tag{28}$$

Now we assume that the incident beam is propagating in the xy plane, the beam can be represented as: $V_0(x,y) = A_0(x,y)e^{j(k_{x0}x+k_{y0}y)}$. The beam after the grating beam is denoted as $V(x,y) = A(x,y)e^{jk_xx+k_yy}$. The transmission function of the grating is [27]:

$$t(x,y) = \frac{V(x,y)}{V_0(x,y)} \tag{29}$$

The phase grating, as mentioned before, is modulating the phase term. So the transmission function can be written as:

$$t(x,y) = e^{j\Delta\varphi(x,y)} \tag{30}$$

As indicated by its name, the Fourier phase grating means the phase term of the transmission function is obtained from the expansion of the Fourier series, and the structure of the grating is designed by optimizing the coefficients in front of each Fourier series term [28]. Now we only consider a 1-D Fourier phase grating, there is:

$$\Delta\varphi(x) = \sum_{n=1}^{N} a_n \cos\left(n\left(\frac{2\pi x}{D}\right)\right) \tag{31}$$

where the unit cell is from $-\frac{D}{2}$ to $\frac{D}{2}$, and a_n are the key parameters which determine the

structure of the grating. The transmission function becomes:

$$t(x) = e^{j\sum_{n=1}^{N} a_n \cos\left(n\left(\frac{2\pi x}{D}\right)\right)} \tag{32}$$

For N=1, it becomes the sinusoidal phase grating, which has a transmission function of $t(x) = e^{ja\cos\left(n\left(\frac{2\pi x}{D}\right)\right)}$. The far-field of this sinusoidal phase grating is:

$$U(\theta) = U_0 \sum_{q=-\infty}^{\infty} J_q(a)\delta\left(\theta - q\frac{\lambda}{D}\right) \tag{33}$$

where $J_q(\cdot)$ denotes the Bessel function of the first kind of order q. So the phase modulated field in N>1 Fourier phase grating plane can be written as:

$$U_0 e^{j\Delta\varphi(x)} = U_0 \prod_{n=1}^{N} e^{ja_n \cos\left(n\frac{2\pi x}{D}\right)} \tag{34}$$

And the far-field for the N>1 Fourier phase grating is:

$$U(\theta) = U_0 \times \otimes_{n=1}^{N} \left[\sum_{q=-\infty}^{\infty} J_q(a_n)\delta\left(\theta - qn\frac{\lambda}{D}\right)\right] \tag{35}$$

where $\otimes_{n=1}^{N}$ stands for multiple convolution. The Fourier coefficient a_n will be chosen to define a grating that can generate a desired far-field beam pattern. However, the Eq.(35) is not able to be inverted to calculate the a_n analytically. So an iterative method, like the numerical Fast Fourier Transform (FFT), will be use to find the a_n. More details about finding these parameter a_n can be referred to the MSc thesis work by Yuchen Luo [29].

Once we obtain the coefficients a_n, the phase difference $\Delta\varphi(x)$ is known. Assuming the incident beam normally incidents on a reflective grating, the path difference according to the Eq.(28) can be expressed in the term of phase difference:

$$\Delta l = \frac{\lambda\Delta\varphi(x)}{4\pi} = \frac{\lambda}{4\pi}\sum_{n=1}^{N} a_n \cos\left(n\left(\frac{2\pi x}{D}\right)\right)$$

(36)

This path difference is also the depth of the each unit cell, which is a function of x-axis position. Figure 20 illustrates an example of a 1-D grating structure. For an arbitrary incident angle incident, the grating can still work by a compensation in its working frequency [29].

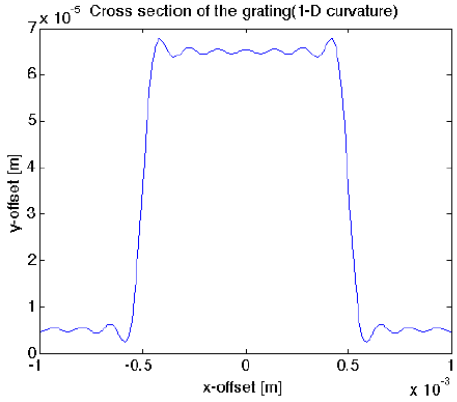

Figure 20. The structure of a 1-D Fourier phase grating unit cell. y-offset is the depth which is determined by the x-offset as the Eq. (36). Figure from [29].

Thanks to the collaboration with Yuchen Luo, I have two Fourier phase gratings which work at 1.4 and 4.7 THz with an incident angle of 25deg. The performances of these two gratings, and their application in receiver array will be further characterized in the Chapter V.

3.2 Angular Distribution of the Fourier Phase Grating

Among all performance parameters of the Fourier phase grating, there is one which determines the optical path design of the LO, that is the angular distribution (also known as the emergent angle), as shown in the Figure 21.

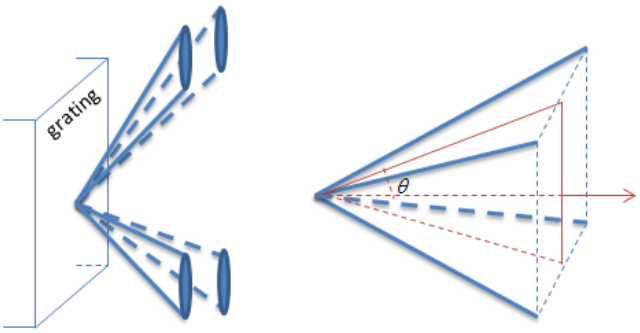

Figures 21. Angular distribution of a 2×2 Fourier phase grating. The emergent angle is defined from one of the first mode beams to the normal direction of the grating surface.

The emergent angle θ is determined by the unit cell size D, the mode order q and the wavelength λ:

$$\sin\theta = q\frac{\lambda}{D} \tag{37}$$

Since we only consider the first order mode, the emergent angle $\theta = \arcsin(\frac{\lambda}{D})$. This angle plays a vital role in designing the LO optical path. Due to manufacturing reasons, the real angle will not be the exactly the same as the theoretical value. This will be presented in the Chapter V as well.

IV

Hot Electron Bolometer Heterodyne Receiver

4.1 Receiver Overview

Terahertz heterodyne receiver has structure similar to a traditional receiver used in the microwave frequency range, especially to the radar system or other scattering communication system. Figure 22 is the one pixel block diagram of the terahertz heterodyne receiver array used in this thesis.

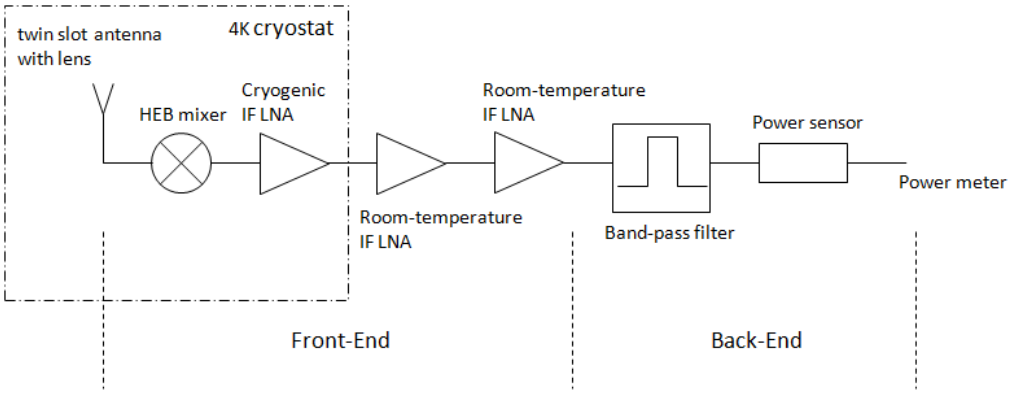

Figure 22. The block diagram of one pixel in the receiver array. The bandwidth of the cryogenic amplifier is 0.5 - 9 GHz, and the gain is around 36dB. The bandwidth of two room temperature amplifiers are 0.1 - 6GHz and 0.1 - 8 GHz respectively, and the gain are around 35dB and 30dB. The band-pass filter has a center frequency of 1.5 GHz and ~ 90 MHz bandwidth in noise temperature and stability measurement. In IF measurement, the band-pass filter is replaced by a spectrum analyzer.

The terahertz signal and LO signal are coupled by a beam splitter and then captured by the twin slot antenna. Then two signals are mixed by the HEB mixer. The output IF signal is amplified by a cryogenic IF low noise amplifier (LNA) and two room temperature IF LNAs. The IF bandwidth of the receiver is limited by the HEB itself, which is always smaller than the bandwidth of these IF amplifiers. Then, for characterization purposes only, the amplified signal passes through a band-pass filter, usually with a bandwidth of ~ 90 MHz and a center frequency of 1.5 GHz. This is to filter out the signal we are not interested in. Finally a power sensor is used to measure this IF signal and displayed on the power meter.

For any terahertz heterodyne receiver, there are three primary parameters which are important for evaluating the receiver performance: noise temperature, IF bandwidth and Allan variance time (stability). The noise temperature determines the minimum signal which can be detected by this receiver, the IF bandwidth indicates the detectable frequency range, while the Allan variance time

remarks the stability of the receiver, and determines the integration time.

4.2 Noise temperature conception and its measurement

4.2.1 Callen and Welton Description

The noise temperature (T_N) is a way to express the level of the noise power introduced by a component or source. For any component, the noise temperature can be expressed as:

$$P_N = kT_N \tag{38}$$

where k is the Boltzmann's constant, and P_N is the noise power per bandwidth. According to the Planck law, the radiated thermal power of a passive resistor (or blackbody) at a certain frequency f per unit bandwidth is [30]:

$$\mathrm{P} = \frac{\mathrm{hf}}{\exp\left(\frac{\mathrm{hf}}{\mathrm{kT}}\right)-1} \tag{39}$$

where h is the Planck's constant and T is the physical temperature of that passive resistor. In most electrical engineering work, the f and T satisfy the condition: $hf \ll kT$, then a so called Rayleigh-Jeans limit can be applied. This RJ law states that the thermal power radiated per unit bandwidth by a passive resistor is:

$$\mathrm{P} \approx \mathrm{kT} \tag{40}$$

This is actually a linear expansion of the exponent in Eq.(39). It indicates that in this situation, the noise temperature T_N simply equals to its physical temperature T.

Now if we want to calculate the radiated power per unit bandwidth of a passive resistor at lower temperature and higher frequency, the RJ-limit does not apply any more since $\mathrm{kT} \not\gg \mathrm{hf}$ [31]. So the radiated noise power of a passive resistor should be written in the form of Eq.(39) . In addition, another term should be also considered if we measure this power using a heterodyne receiver, which is called quantum noise with a noise power per unit bandwidth of $\mathrm{hf}/2$ (W/Hz). This power is associated to the measurement of any EM radiation, but not the real power transferred from the source to the detector [30]. Thus, the measured radiated power from a passive resistor is:

$$\mathrm{P_{CW}} = \frac{\mathrm{hf}}{\exp\left(\frac{\mathrm{hf}}{\mathrm{kT}}\right)-1} + \frac{\mathrm{hf}}{2} \tag{41}$$

This is also called Callen and Welton description. If we represented this power in terms of

temperature, which is also known as the effective temperature, then there is:

$$T_{CW} = \frac{hf}{k}\frac{1}{\exp\left(\frac{hf}{kT}\right) - 1} + \frac{hf}{2k} \tag{42}$$

4.2.2 Receiver noise temperature measurement

To measure the noise temperature of the receiver, we firstly regard the whole receiver itself as an ideal amplifier, which adds its own noise power in the input signal and amplified them together, as illustrated in the Figure 23.

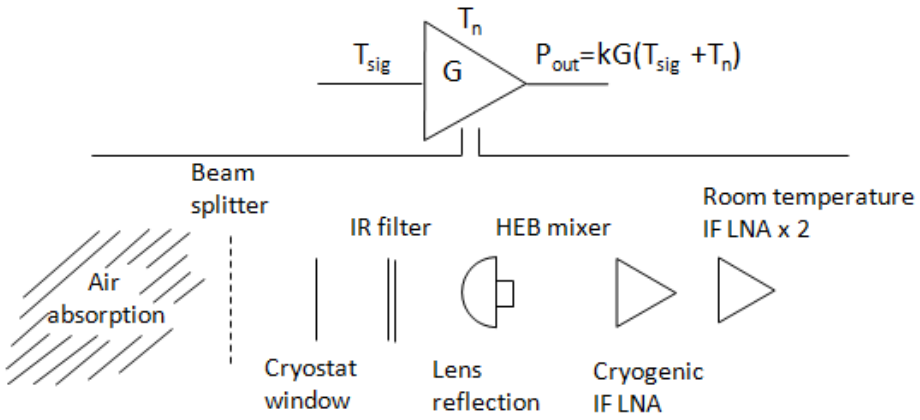

Figure 23. Illustration of regarding the receiver as an ideal amplifier. The whole receiver includes all the components from the air absorption to the back end of the receiver, which will introduce noise.

Then the output power per bandwidth of this receiver is:

$$P_{out} = Gk\left(T_{sig} + T_n\right) \tag{43}$$

where G is the gain of the receiver, T_{sig} is the input signal power in term of noise temperature, T_n is the receiver noise power in terms of noise temperature. If we connect two different temperature loads (hot and cold) at the input of the receiver, we could derive the T_n as a function of $P_{hot\ out}$, $P_{cold\ out}$ and $T_{sig\ hot}$, $T_{sig\ cold}$:

$$T_n = \frac{T_{hot\ load} - YT_{cold\ load}}{Y - 1}$$

$$Y = \frac{P_{hot\ out}}{P_{cold\ out}} \tag{44}$$

where $P_{hot\ out}$ and $P_{cold\ out}$ are the output power of the receiver with hot and cold load, which are measured by the power-meter. $T_{hot\ load}$ and $T_{cold\ load}$ are the effective temperature of the hot and cold load, calculated using Eq. (42) from Callen and Welton description.

As shown in the Figure 23, the receiver noise temperature depends largely on the components in the receiver. For example, the reflection losses from the lens is a very significant factor which will influence the receiver noise temperature. Using the AR coating, the noise temperature can be improved by about 30%.

Moreover, if we would like to characterize the noise temperature of an HEB mixer itself (or intrinsic mixer noise temperature), we need to subtract all optical losses and air absorption. Otherwise, the measurement condition should be mentioned in order to relatively characterize the HEB mixer performance. In this thesis, all measurements are carried out under the following conditions, as summarized in Table III, unless otherwise specified. Chapter VII will present the measured noise temperature results.

Table III. Measurement Condition

	Type	**Losses (dB)**
Beam splitter	6um Mylar	0.25
Cryostat window	1.2 mm UHMW-PE	1
IR filter	QMC metal mesh W907	0.2
Lens	10mm uncoated elliptical lens	1.5
	10mm coated elliptical lens	1
Air	20 cm, ~30% humidity	0.2
Total		**3.15/2.65**

4.3 IF Bandwidth and Measurement

The IF bandwidth actually can be described in terms of either IF noise bandwidth or IF gain bandwidth. In this thesis, we will only concentrate on the IF noise bandwidth, since the noise temperature is key parameter in evaluating the receiver performance.

The noise temperature of the receiver, as indicated by the Eq. (42)(44), is a function of the frequency. Thus, it is also a function of the IF frequency. The IF noise bandwidth is defined as the IF frequency point where the noise temperature is doubled with respect to its minimum noise temperature in the limit of zero IF frequency. Otherwise, we can also find the IF frequency range where the noise temperature is below a certain value. This indicates the frequency range where the HEB mixer can detect without suffering from a high noise.

The IF noise is calculated using the same method as calculating the noise temperature at a certain frequency point. However, the band-pass filter, power sensor and power meter are replaced by a spectrum analyzer which can display the fill IF range of 7 GHz. This IF frequency range is limited only by the frequency range of the cryogenic LNA. The result of the IF bandwidth will also be presented in the Chapter VII.

4.4 Allan variance time conception and measurement

4.4.1 Allan variance conception

Allan variance measurement is a standard way to characterize the stability of the radio-astronomy instrument by discriminating various noise terms [32]. The term Allan variance is introduced by Allan in 1966 [33]. We can understand the Allan variance as the ordinary statistical variance of the difference of two continuous measurements [34].

Assuming we measured a set of continuous data $s(t)$, and the output is now integrated for time interval T to improve the stability. Then there is

$$x(T,t) = \frac{1}{T}\int_{t-T}^{t} s(t')dt' \tag{45}$$

Considering two adjacent averaged signals: $x(T,t)$ and $x(T,t+T)$. The difference of these two measurements is:

$$d(T) = x(T,t+T) - x(T,t) \tag{46}$$

The variance $(\sigma^2(T))$ of $d(T)$ can be written as:

$$\begin{aligned}\sigma^2(T) &= < (d(T) - < d(T) >)^2 > \\ &= < d(T)^2 > - < d(T) >^2\end{aligned} \tag{47}$$

The Allan variance $(\sigma_A{}^2(T))$ can be then defined as:

$$\begin{aligned}\sigma_A{}^2(T) &= \frac{1}{2}\sigma^2(T) \\ &= \frac{1}{2}(< d(T)^2 > - < d(T) >^2)\end{aligned} \tag{48}$$

Since in astronomy observation, the signal is always embedded in the noise, it is very normal that the expectation value of the $d(T)$ is zero [33]. Then the Eq.(48) becomes:

$$\sigma_A{}^2(T) = \frac{1}{2} < d(T)^2 > \tag{49}$$

4.4.2 Allan variance measurement

To characterize the stability of the whole receiver array, we will investigate the Allan variance time of the output power. In a real measurement, the data can only be discrete and finite [34]. For example, the sampling power data is $n(i)$ with a sampling rate of $1/t$ Hz and number of N. Then, as indicated by the Eq.(45), we would like to integrate in a time period of τ, where $\tau = kt$ ($k = 1,2,...,$ N-1), to improve the stability. Assuming M is the number of groups under a

certain integration time period τ. Then the expectation $n(\tau, i)$ of each group is:

$$M = \left[\frac{N}{k}\right]$$

$$n(\tau, i) = \frac{1}{(k+1)} \sum_{k(i-1)+1}^{ik+1} n(i), \quad i = 1,2, \dots, M \tag{50}$$

where $[\cdot]$ denotes the largest integer which is smaller than N/k (usually when k becomes larger, the Allan variance becomes less reliable, since M becomes smaller):

So the difference between two adjacent expectation of integrated data is:

$$d(\tau, i) = n(\tau, i+1) - n(\tau, i), \quad i = 1,2, \dots, M-1 \tag{51}$$

So as defined in the Eq. (48), the Allan variance time for discrete signal is:

$$\sigma_A{}^2(\tau) = \frac{1}{2(M-1)} \sum_{i=1}^{M-1} (d(\tau, i) - < d(\tau, i) >)^2$$

$$< d(n) > = \frac{1}{M-1} \sum_{i=1}^{M-1} d(\tau, i) \tag{52}$$

As indicated in the Eq. (49), the mean value can be regarded as zero when the input the signal is very small comparing to the noise. So Eq. (52) can be written as:

$$\sigma_A{}^2(\tau) = \frac{1}{2(M-1)} \sum_{i=1}^{M-1} \big(d(\tau, i)\big)^2$$

$$= \frac{1}{2(M-1)} \sum_{i=1}^{M-1} [n(\tau, i+1) - n(\tau, i)]^2 \tag{53}$$

Figure 24 illustrates the calculation process of Allan variance time from the raw sampling data.

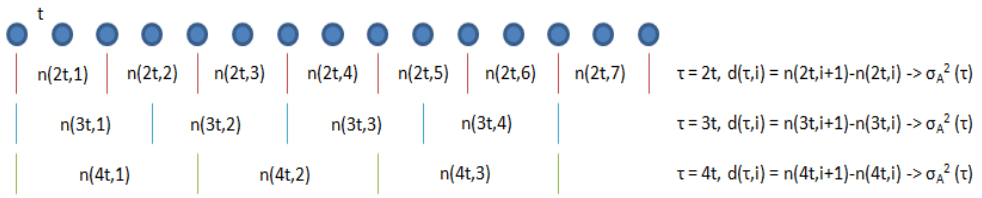

Figure 24. Allan variance calculation process. Blue points denote the raw sampling data. They are sampled at a rate of t ms. Red, blue and green groups indicate that we integrate for 2t, 3t, and 4t ms respectively. The n(at,b) is the average value of the integrated data

According to the [32][34], the low frequency noise power spectrum can be expressed as: $S(f) \propto 1/f^{\alpha}$, with $1 \leq \alpha < 3$ *and* $\alpha = 0$. Table IV summarizes the source for different noise types and their time domain figures [35].

Table IV. Spectrum, source and time domain figures for different noise components

	Spectrum	Source	Time domain figure
White Noise	$S(f) = 1$	Completely uncorrelated noise	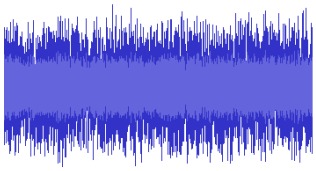
1/f Noise	$S(f) = 1/f$	Mainly comes from the electronic components. The influence of atmospheric fluctuations may have the same characteristics.	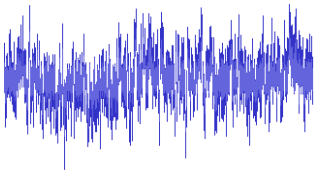
Drift Noise	$S(f) = 1/f^2$	Mainly comes from the drift in the bias points of the HEB mixer.	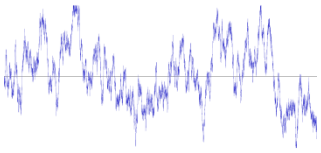

Corresponding to the S(f), the Allan variance is given by $\sigma_A{}^2(t) = t^{\alpha-1}$, where t is the integration time. So for a noise spectrum which contains white noise, 1/f noise and drift noise, the Allan variance time can be expressed as:

$$\sigma_A{}^2(t) = at^{\beta} + b + \frac{c}{t}, \quad \beta = \alpha - 1 \text{ and } 1 \leq \beta < 2 \tag{54}$$

As indicated by the relation between β and α, the first term in Eq. (54) corresponds to the drift noise, the second term corresponds to the 1/f noise, and the third term corresponds to the white noise.

We can also find that for short integration time, the white noise term (c/t) will dominate the

Eq. (54). The Allan variance will decrease as a function of t^{-1}. For long integration time, the drift noise term (at^{β}) will dominate the Allan variance, which results in an increase with a slope β. At some points between the short and long integration time, the 1/f noise will be the dominator. And the Allan variance time will become flat as a function of time. Figure 25 gives an illustration of Allan variance time for different noise types.

Besides using Allan variance data to distinguish the noise components present in a given signal, we can also use it to determine the optimum integration time. As indicated by the Eq. (50), we always do an integration to the data set to get a more stable result. However, a longer integration time does not always ensure a higher signal to noise ratio. Since the integration only removes the white noise, but it does nothing to the 1/f noise and drift noise. If there is only white noise component, the variance of the output power will be a function of the inverse of the integration time, also known as the radiometer equation..

$$\sigma(\tau)^2 = \frac{\mu^2}{B\tau} \tag{55}$$

The result will be more stable when the integration time is longer. So the best integration time should be the last point where the white noise still dominates in the noise spectrum. After this point, the 1/f noise or drift noise will become the dominator. And longer integration does not help to any of these two noises.

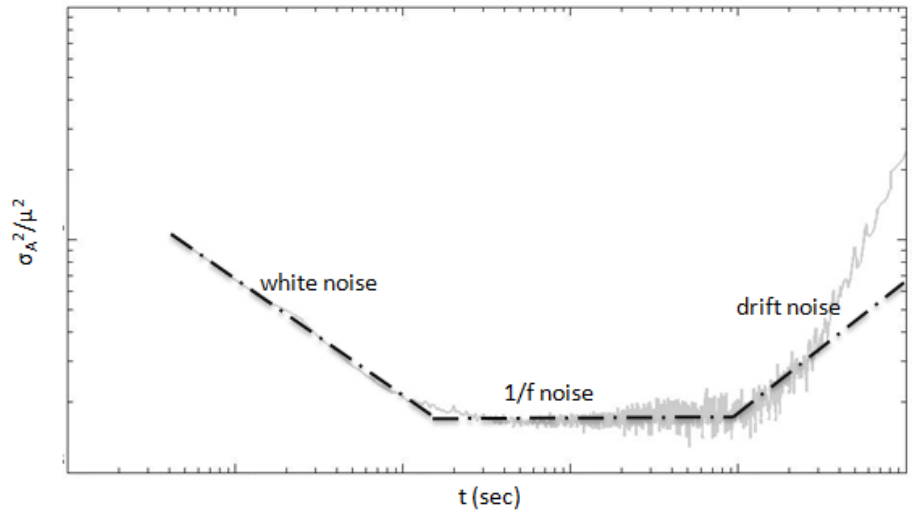

Figure 25. Allan variance time as a function of integration time. The Allan variance time is normalized to the mean value of raw sampling data. The gray curve is the Allan variance time of one pixel in the receiver array, obtained from Eq. (53). Black curve is an illustration of different noise components in terms of Allan variance time. In the end of drift noise part, the measured Allan variance may not be reliable since the number of data group is not enough.

Eq.(53) is the formula to calculate the Allan variance for a single channel in our receiver array at a certain IF frequency, which is also known as the total power Allan variance. It indicates the absolute stability of the channel. Another type of Allan variance is called spectroscopic Allan

variance, which is the Allan variance of the difference of two IF channels set to different frequencies. It gives the relative stability between channels in an IF band [32]. Due to the limitation of the number of IF chains in our measurement setup, this thesis will only focus on total power Allan variance.

4.5 Current Stability Method

As shown in the Figure 25, the Allan variance time becomes even worse if the drift noise dominates in the noise spectrum, which means the long integration time even results in a less stable result. So the drift noise becomes a key factor which limits the integration time. Since the drift noise mainly comes from the drift in bias points of the HEB mixer, we need to stabilize the bias points, which are bias voltage and current.

The bias voltage is added by the bias supply box, which is verified to be stable enough. The bias current, however, is largely determined by the LO power and signal power which are very unstable. Actually there are some arguments around this statement that some people think the noise in HEB mixer itself is the main source for the unstable current. But in the Chapter VII we will prove that the unstable current is mainly caused by the unstable LO power, instead of the HEB mixer itself.

One way to stabilize the current is to stabilize the incident LO power by using a voice coil controlled arm with absorber [36], as shown in the Figure 26.

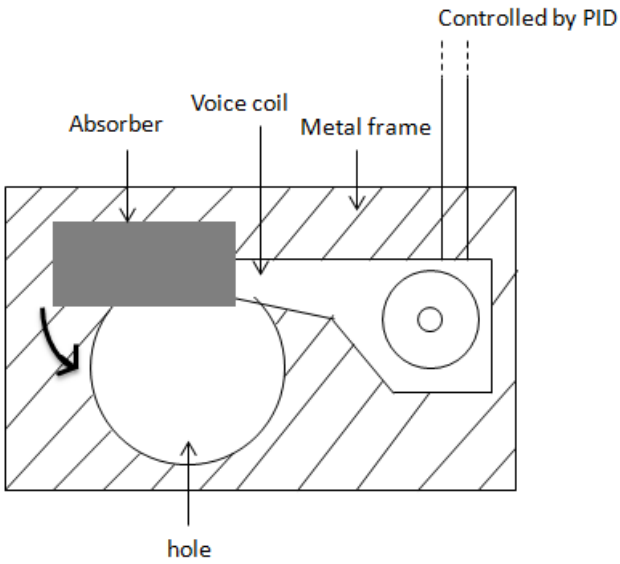

Figure 26. Illustration of the voice coil arm with absorber. In open state, the LO beam can fully pass through the hole, while in close state, the absorber can fully block the LO beam. The voice coil arm is driven by the PID controller in a state between the fully open and fully block state to stabilize the incident LO power, and thus stabilizes the HEB mixer current.

The voice coil is controlled by a PID controller. The PID input is the read out DC current of the HEB mixer, and PID output is the current which can drive the voice coil. When the LO power increases (decreases), the current of the HEB mixer will decrease (increase) since the resistance region becomes larger (smaller). The change in the HEB current will be sensed by the PID controller, and it will move the voice coil arm to partially block (unblock) the hole to decrease

(increase) the incident LO power. In this way, the incident power of the LO beam is controlled, and the current of the HEB mixer is stabilized. This process is illustrated in the Figure 27a.

For a one pixel system, this method has already been proved to be very effective. It can maximally enable a 50 times improvement in the Allan variance time comparing to the un-stabilized one [36]. Since the sub LO beams in our array are duplicated from the original beam by the grating, we would like to investigate that whether we can stabilize two pixels using one PID controller, as shown in the Figure 27b. The result will be summarized in the Chapter VII.

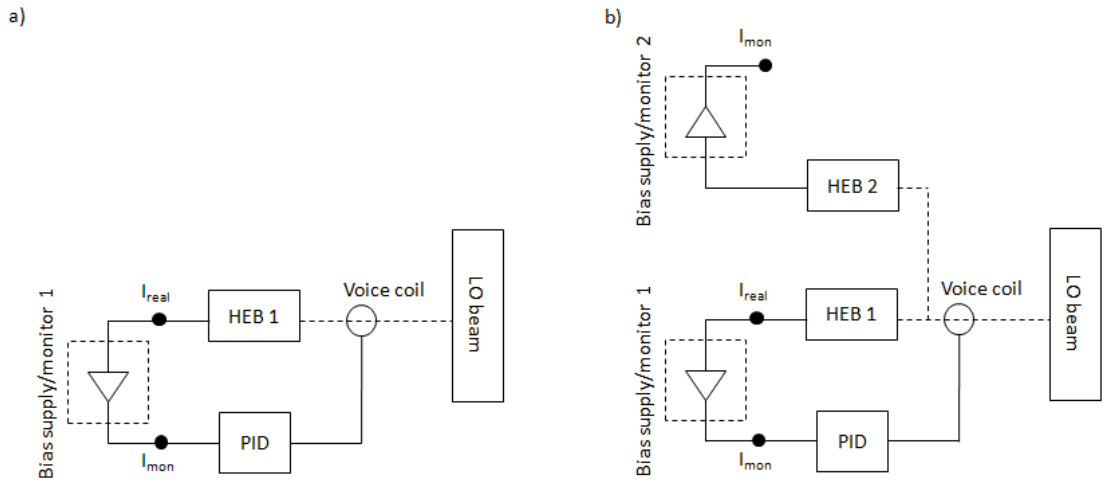

Figure 27. a: PID stabilization process for one pixel system. The real current is read out through the bias supply, which can be simplified as an amplifier; b: Idea of stabilizing two currents using one PID controller.

V

Fourier Phase Grating Characterization and LO Optical Path Design

5.1 Fourier Phase Grating Performance

Two Fourier phase gratings which are designed for 1.4 THz and 4.7 THz with an incident angle of 25deg are shown in the Figure 28. The physical dimensions [29] of them are summarized in the Table V.

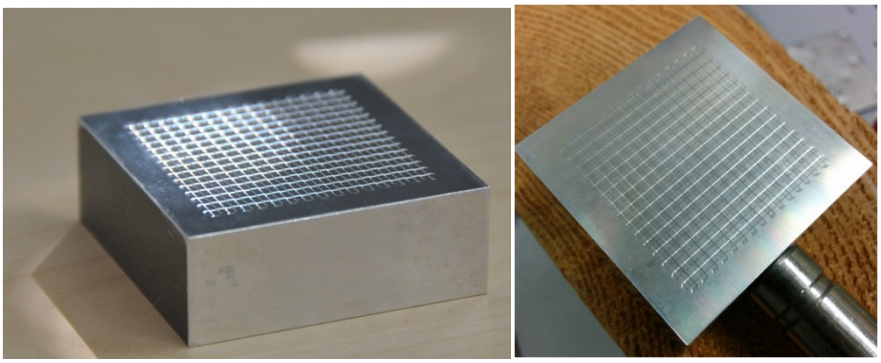

Figure 28. Photos of 1.4 THz (left) and 4.7 THz (right) Fourier phase grating.

Table V. Physical dimension of the 1.4 THz and 4.7 THz Fourier phase grating

	Maximum groove depth (um)	**Minimum curve radius (mm)**	**Unit cell size (mm×mm)**	**Number of unit cells**	**Grating size (cm×cm)**
1.4 THz	130.2	0.1	2×2	225	3×3
4.7 THz	34.8	0.34	2×2	225	3×3

The two gratings have the same unit cell size. According to the Eq. (37), the angular spacing for each grating is: 6.1deg (1.4 THz) and 1.82deg (4.7 THz) respectively. In order to verify this, we use a XYZ scanner to scan the sub-LO beams pattern at different distances from the grating. The scanner has a maximal scanning range of 90mm by 90mm. The beam power is modulated by a chopper with a frequency of ~80Hz, and it is read out through a pyro-electric THz detector. Figure 29a shows the scanning setup.

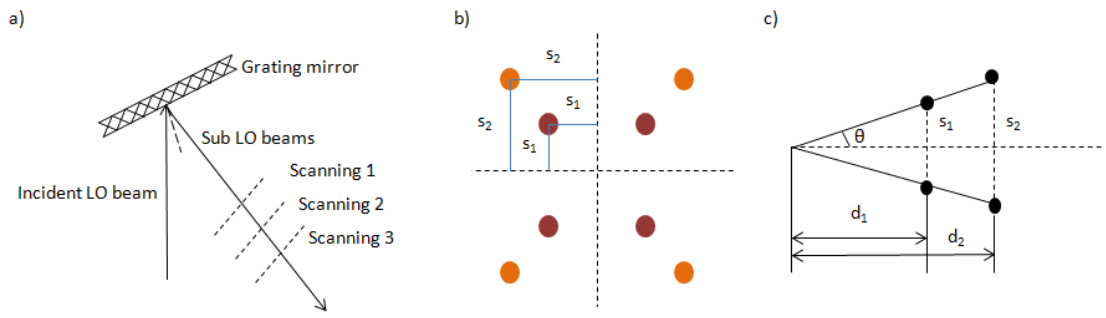

Figure 29. a: Set-up for measuring the angular distribution of the sub-LO beams; b: Geometric model for the 2×2 sub LO beams at different scanning distances; c: Geometric model for the side view of 2 sub LO beams at different scanning distances.

Figure 29b and c are the geometric models to calculate the emergent angle θ. Based on this geometry model, the θ is:

$$\theta = \arctan \frac{(s_2 - s_1)}{(d_2 - d_1)} \tag{56}$$

Figure 30 is the measurement results for 1.4 THz and 4.7 THz grating. The calculated emergent angle is 5.7 deg and 2.0 deg respectively.

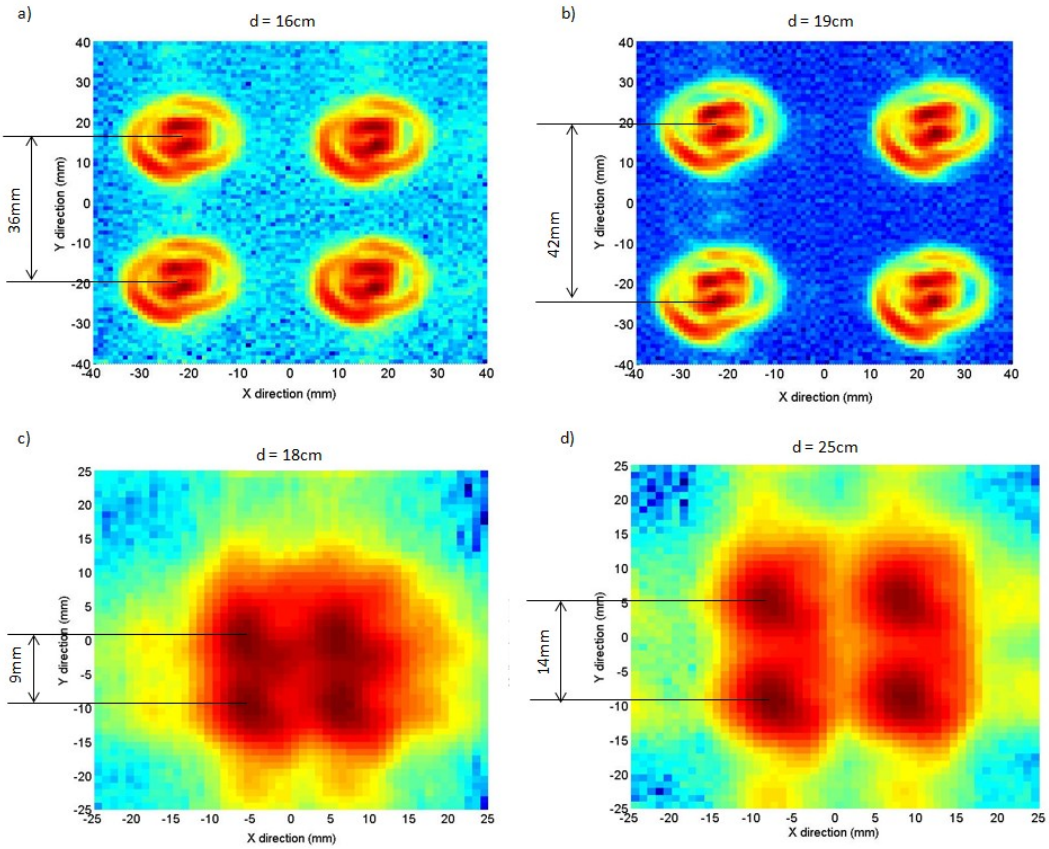

Figure 30. a and b: measured results for 1.4 THz grating. a is measured at a distance of 16cm and

the spacing between two beams is 36mm. b is measured at a distance of 19cm and the spacing between two beams is 42mm; c and d: measured results for 4.7 THz grating. c is measured at a distance of 18cm and the spacing between two beams is 9mm. d is measured at a distance of 25cm, and the spacing between two beams is 14mm.

The calculated emergent angles for two gratings are very close to the theoretical values: 6.1 deg for 1.4 THz and 1.82 deg for 4.7 THz. From the figure, we can also find that the four sub LO beams are identical to each other, which proves that the grating indeed just duplicates the original beam.

5.2 LO optical path design for 1.4 THz 2×2 array

The emergent angle for the 1.4 THz grating, as indicated above, is about 5.7 deg. The spacing between each pixel in the mixer block, as indicated in the Chapter II, is 12 mm. So if we would like to have a 2×2 LO array which has a spacing of 12mm, the distance from the mixer block plane to the grating should be around 60mm. However, due to the fact that there is a certain distance from the cryostat window to the HEB mixer block, 60mm distance is not enough to place the cryostat in front of the grating. Thus, we would like to have four parallel sub LO beams which can enable enough space to place the cryostat. Figure 31 is the designed LO optical path which can enable four parallel beams:

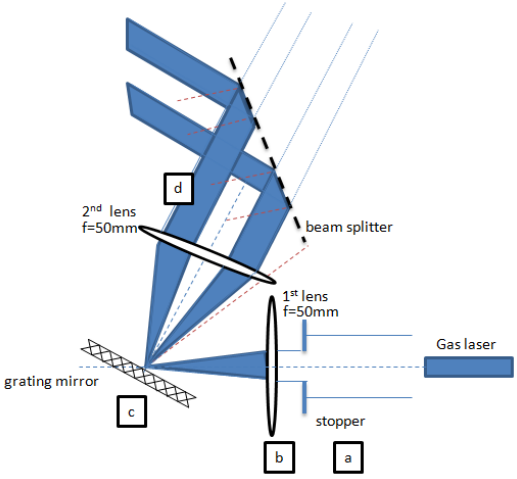

Figure 31. LO optical path for 2×2 array. The two lenses are identical and have a focal length of 50mm. This is to make the spacing between each sub LO beam is 12mm and parallel to each other. An aperture stop is used before the 1st lens to eliminate the rings around the original beam and to make the beam clean. A beam splitter is used to couple the LO beam and signal beam.

The sub LO beam patterns at position a, b, c and d are shown in the Figure 32.

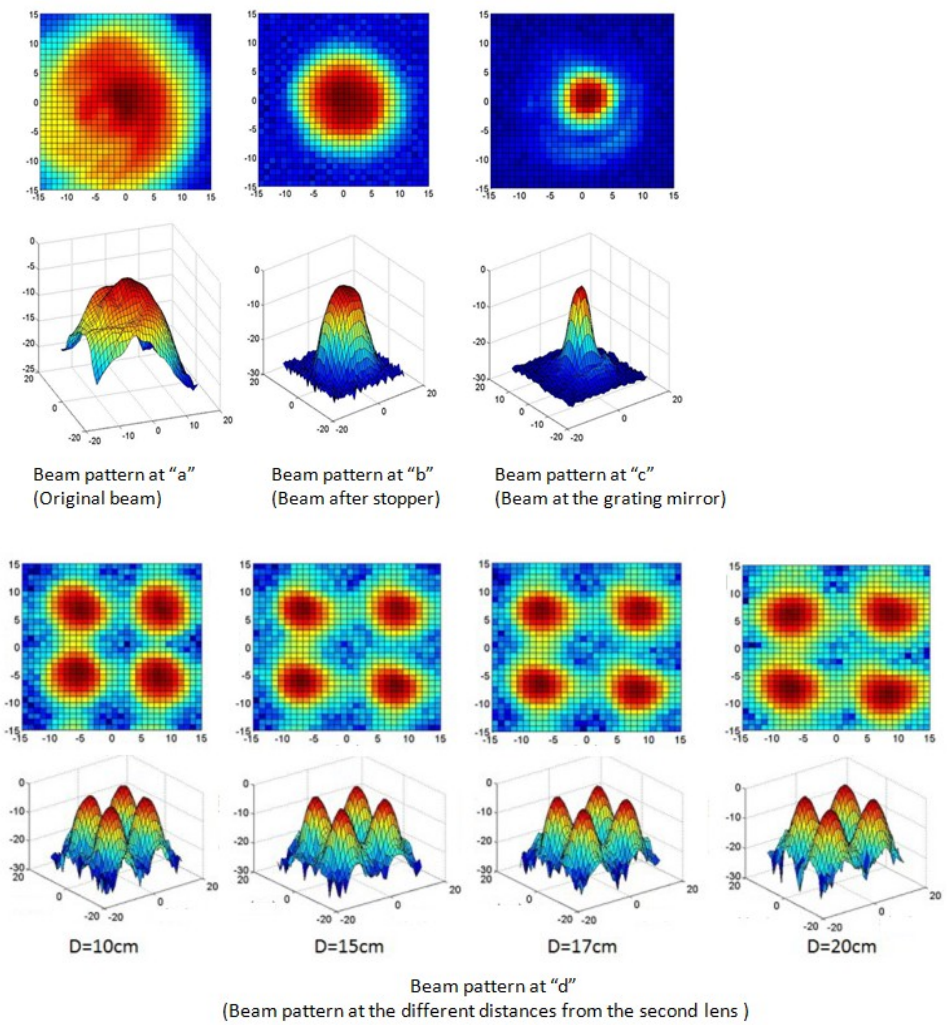

Figure 32. Beam patterns at different positions of the LO optical path. The scanning resolution is 1mm. The last four figures are measurement results of distance equals to 10cm, 15cm, 17cm and 20cm from the Pyro-electric detector to the second lens. The result indicates that the four beams are parallel to each other, and with a spacing of ~12mm between each other.

The original beam, as shown in the first figure, is not a Gaussian shape beam. So an aperture stop is used to form a cleaner beam. However, this component is not necessary in real application if the original beam is already clean enough. From the last four figures, we can find that the spacing between each sub LO beam is unchanged when the scanning distance increases, which indicates that the four beams are parallel to each other. The spacing between each sub LO beam is around 12mm, which fits the receiver array configuration.

5.3 Phase Grating Efficiency Estimation

As mentioned in Chapter III, the Fourier phase grating can have a very high efficiency which makes it a good candidate for LO multiplexing. The efficiency of this 1.4 THz grating can be estimated by integrating over the whole beam pattern range. The integration is done by adding the pyro-electric detector read out values in all unit cells. The integration results are only the relatively values.

The beam power in b position is 44.15mV in 50mV scale, the power in c position is 13.37mV

in 100mV scale, while the power in d position is 58.24 in 10mV scale. So the transmission efficiency from the "b" to "c" (through the first lens) is:

$$\eta_{b-c} = \frac{13.37 * 100}{44.15 * 50} = 60.5\% \tag{57}$$

The transmission efficiency from "b" to "d" is:

$$\eta_{b-d} = \frac{58.24 * 10}{44.15 * 50} = 26.4\% \tag{58}$$

Since the two lenses are identical, we can assume the second lens has the same transmission property as the first one. So the efficiency of the grating is:

$$\eta = \frac{\eta_{b-d}}{\eta_{b-c}^2} = 72.1\% \tag{59}$$

The absorption by the air might influence this efficiency result. Considering the short air optical path in this design, however, we can neglect this absorption influence. In the Chapter VII we will prove that each sub LO beam has enough power to fully pump the HEB mixer.

VI

Receiver Array and Measurement Scheme

6.1 Measurement Scheme Overview

Based on the previous LO beam distribution scheme, the whole measurement scheme is shown in the Figure 33a and b. All the measurements are performed in air environment, and the measurement devices are summarized in the Table VI.

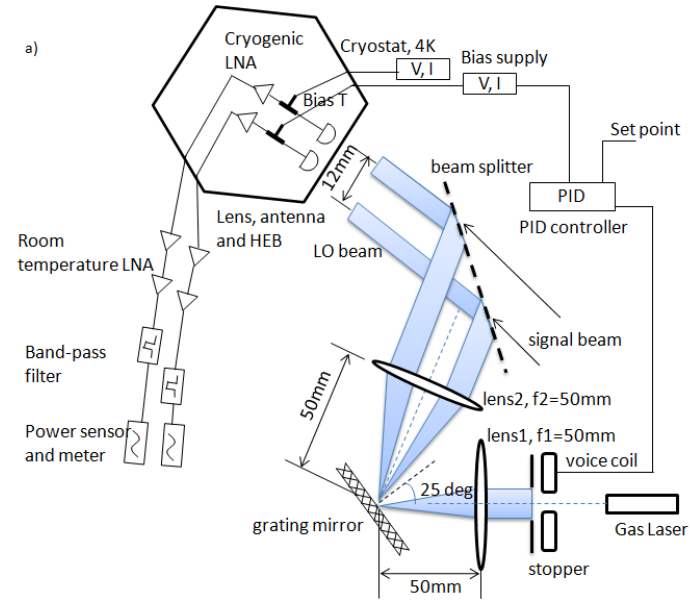

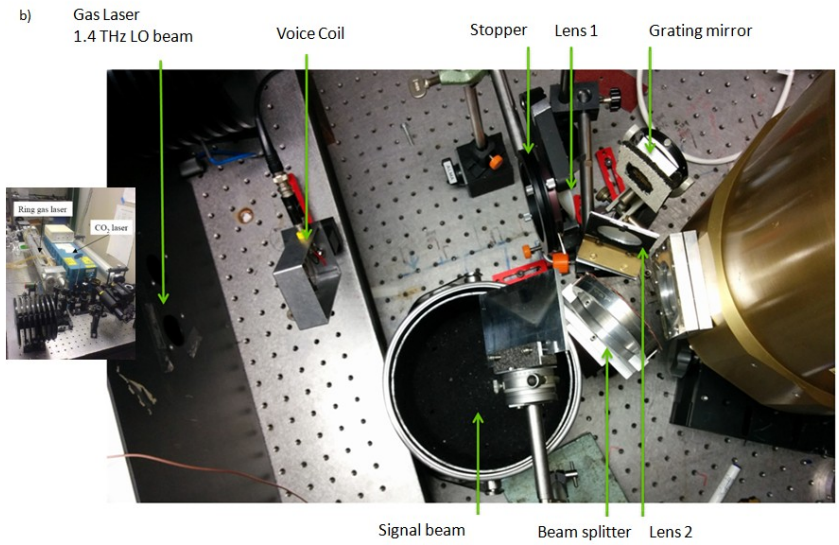

Figure 33. a: Receiver array and measurement scheme. The bias T is used to separate the DC and

AC (IF) signals. The DC signal will be monitored by the bias supply, and read out will be sent to the PID controller to control and stabilize the current. The AC (IF) signal power is detected by the power meter. Only two pixels are drawn in this figure, another two pixels only have the same DC measurement circuits, but without the IF measurement circuits; b: Photo of the measurement setup. The bias supply, PID controller, amplifiers, band-pass filter, power sensor and meter are not shown.

Table VI. Measurement Instruments Summary

Gas Laser	FIR gas laser	**Power meter**	Agilent E4418B Single Channel power meter
Power sensor	Agilent E4412 CW diode power sensor	**Spectral Analyzer**	Rohde & Schwarz Spectrum Analyzer
PID controller	Stanford Research Systems SIM 960 Analog PID controller	**Bias supply**	Bias supply box made by SRON

6.2 DC signal measurement

The DC signal measurement is performed by the bias supply box based on the four-wire measurement method. Four wire measurement is more suitable for small resistance measurement than traditional two wire measurement method. Appendix A.1 summarizes the two measurement methods.

Due to the high static sensitivity of the HEB mixer, a safe switch circuit is applied to avoid the unwanted current when we are not measuring. The safe switch is implemented simply by connecting the HEB mixer with a large resistor when it is not being measured by the bias supply box, instead of letting it be open circuit. The detailed design of the safe switch circuit is presented in Appendix A.2.

6.3 RF signal measurement

The RF signal measurement is mainly the measurement of IF signal power. It is done by using the power meter (noise temperature and Allan variance time) or the spectrum analyzer (IF bandwidth).

When measuring the noise temperature as a function of the bias points (bias voltage and bias current) , the HEB will suffer from a so called direct detection problem [25] if we measured it by directly scanning its bias voltage. This is caused by the direct detection response of the HEB mixer. When the absorbed RF signal power is non-negligible comparing to the sum of the LO power and DC power, the change in RF signal power will change the bias current of the HEB even though the LO and DC power are unchanged. The HEB acts like a direct detector or bolometer in this case, as shown in the Figure 34.

Since the noise temperature measurement, as mentioned in Chapter IV, will use two loads with different temperatures (different RF signal power), the bias current will drift in the measurement due to this direct detection response, and cause incorrect results.

Thus, a new measurement method is applied [37], which is to scan the bias current at different bias voltage points using the voice coil arm together with the PID controller. In this way,

the direct detection problem is eliminated since the voice coil arm can control the LO power to compensate for the RF signal power changes. Moreover, the instability in the LO power is also avoided by using the voice coil arm.

When measuring the Allan variance time, the power meter has to be set at a fast sampling mode. The theoretical sampling rate is 200 Hz, however, the real sampling rate is around 150Hz due to the limitation of the software.

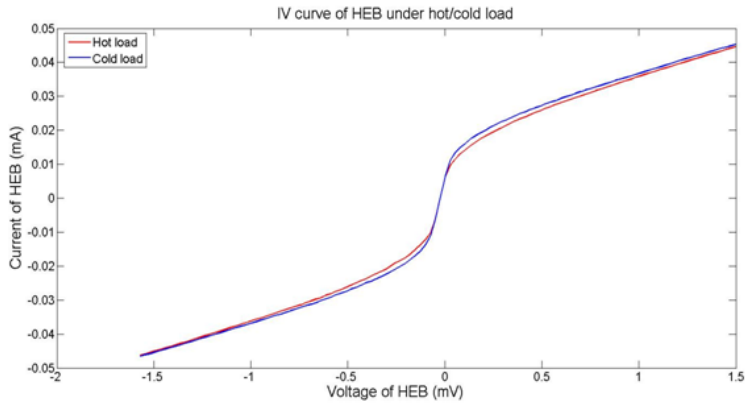

Figure 34. Direct detection of the HEB mixer. The current of the HEB mixer is different when it is connecting with a hot and cold load. This current difference is the response of the HEB mixer to different input signal power, just like a direct detector.

6.4 LabView Controlled RF measurement facilities

All the measurement instruments listed in the Table VI, except the gas laser, are controlled by the LabView through the General Purpose Interface Bus (GPIB) and Data Acquisition (DAQ) board. The connection diagram of entire setup is shown in the Figure 35.

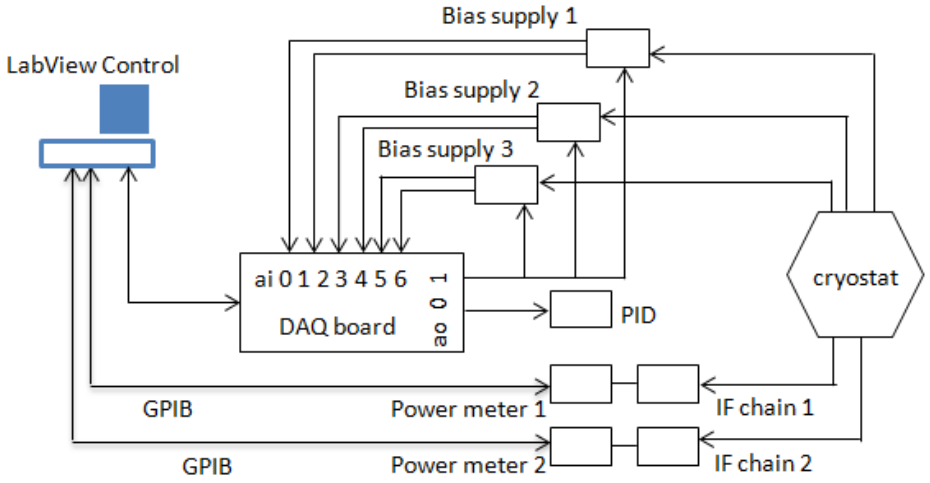

Figure 35. Instruments connection diagram. The ai0 to ai6 ports are the analog to digital ports which are used for reading, while the ao0 and ao1 ports are digital to analog ports which are used for writing. The DAQ board enables the data communication between the computer, bias supply and PID controller. The GPIB connects the power meter and computer directly, and it enables the data communication between them. The arrow indicates the direction of data flow.

The bias supplies and PID controller are connected with the computer through the DAQ board, while the power meters are connected with the computer through the GPIB. Since we have three bias supplies and six analog-to-digital ports (ai0 to ai6) on the DAQ board available, we can only measure the DC performances of three pixels simultaneously (two analog-to-digital ports are needed for one pixel). The last pixel will be measured by switching the bias supply. The sampling rate of the DAQ can achieve 1kHz, which allow us performing a frequency domain measurement up to 500 Hz. In time domain DC signal measurement, the sampling data are summed up and averaged in the computer through LabVIEW program. This will cause the real sampling rate to be slightly less than 1kHz.

Meanwhile, only two IF powers can be measured simultaneously due to the limitation of the IF output ports in our cryostat. The power meter can operate at a low (normal) sampling rate (20Hz or 40Hz) state when performing noise temperature measurement or high sampling rate state (200Hz) when performing Allan variance time measurement. Similar to the DAQ, the real sampling rate will be slight lower than theoretical value due to the data process inside the computer through the LabVIEW software.

VII

Receiver Array Performance Characterization

7.1 IV Curve

The IV curve indicates the state of the HEB mixer, and it is also influenced by the HEB direct detection level. When there is no LO power and the DC power is low, the HEB mixer is in the superconducting state, also known as the un-pumped state. There will be negligible voltage since the resistance is close to zero. When the DC power is high enough, the HEB mixer will become a normal resistor. When the LO power is large enough, the HEB mixer will be fully pumped. In this case, the whole superconducting bridge becomes "hot spot region". The IV curve of the HEB mixer will be a near straight line (like the IV curve of a normal resistor). In a state between the superconducting and fully pumped, the IV curve of the HEB mixer will be non-linear. The state where the HEB mixer exhibits minimal noise temperature is also called the optimal pumped. Figure 36 shows the IV curves of the four pixels under no LO power, fully pumped and optimal pumped situation.

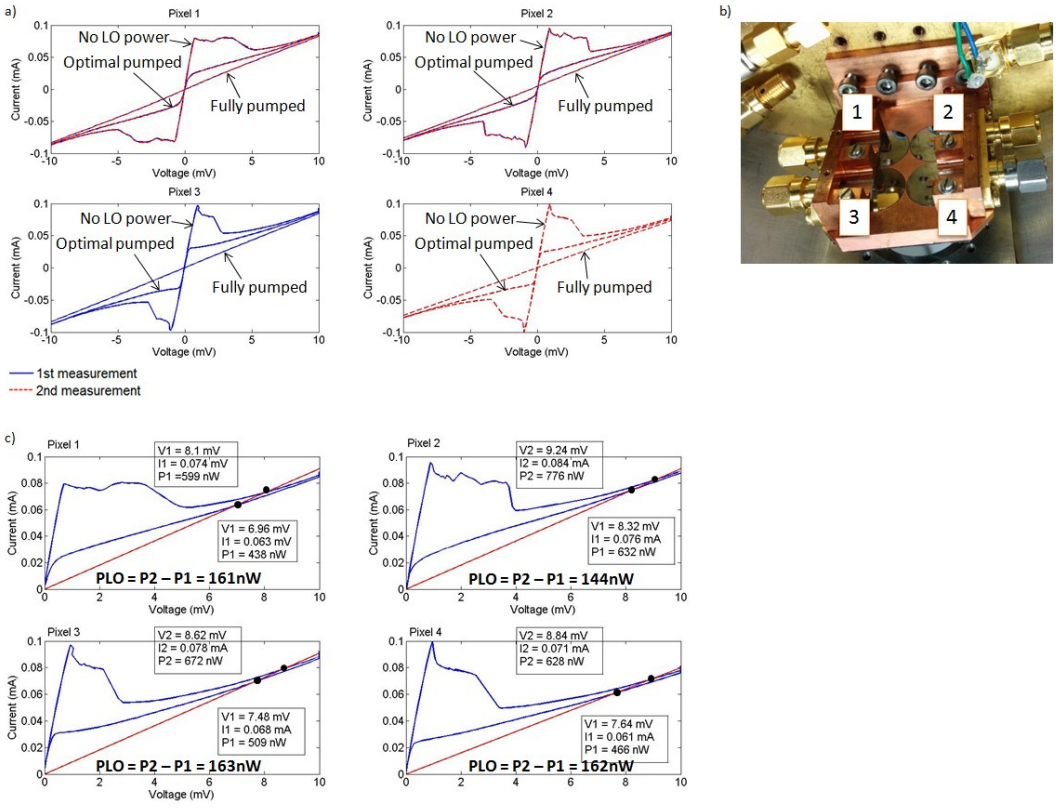

Figure 36. a: IV curves of four pixels under no LO power, optimal pumped and fully pumped states. Blue curve is the first three pixels measurement result. Red dotted curve is the second three

pixels measurement result. Pixel 1 and 2 serve as references in second measurement; b: Configuration of four pixels; c: Optimal LO power needed for each pixel. The red straight line is the IV curve of a normal resistance. It intersects with the un-pumped and optimal pumped IV curve. The optimal LO power is calculated by subtracting the power value at the two intersected points.

When there is no LO power, four pixels all exhibit a very sharp slope in IV curve within a bias voltage range of -0.8mV to 0.8mV. However, this IV curve does not represent a completely superconducting state. This is due to a small series resistance from the contact pads. The four fully pumped results indicate that each sub LO beam power is high enough to pump the whole HEB mixer to normal resistance state. By reducing the LO power to a certain level, the four pixels can be optimally pumped simultaneously. The optimal LO power can be calculated from un-pumped and optimal pumped IV curves. The LO power for each pixel to be optimal pumped is: 161nW, 144nW, 163nW and 162nW respectively. Assuming the beam splitter has a reflection efficiency of 10%, and based on the estimated transmission efficiency of the whole LO optic path (Eq. (58)), the total required power of the incoming LO source should be ~ 25μW to optimal pump 4 pixels.

Although these four HEB mixers have the same physical dimensions as shown in the Table II, the IV curves and critical currents are still slightly different from each other. However, this only makes small difference in optimal pumped power required by each pixel. And as shown later, it also does not affect the noise temperatures significantly.

7.2 Noise Temperature Performance

As mentioned in Chapter IV, the noise temperature is one of the most important parameters for evaluating the HEB mixer performance in terms of sensitivity. We measured the receiver noise temperature as a function of bias current at different bias voltage points for two pixels with uncoated lenses, as shown in the Figure 37. The whole measurement is carried out in the array, and is based on the use of Fourier phase grating.

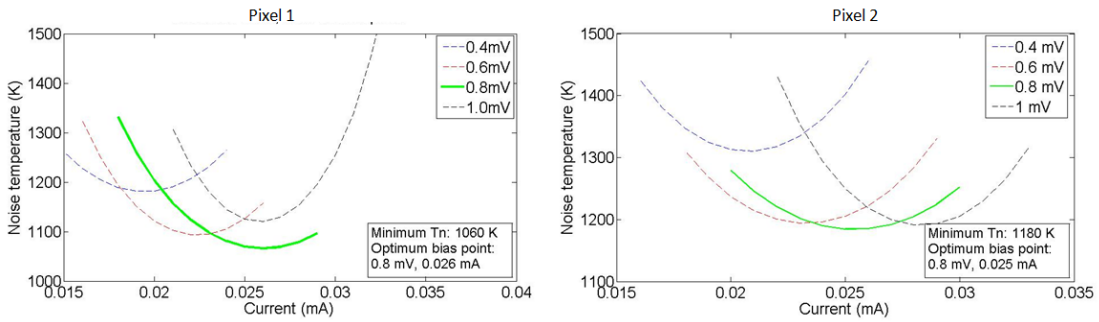

Figure 37. Noise temperature vs. current at different bias voltages for two pixels with uncoated lenses. Green curve indicates the noise temperature at optimal bias voltage. The minimum noise temperature for pixel 1 is about 1060K, at (0.8mV, 0.026mA), for pixel 2 is about 1180K, at (0.8mV, 0.025mA).

The two pixels have similar minimum noise temperature and optimal bias point. We also notice that the noise temperature does not change much from the minimum point in a certain range. For example, the noise temperatures for pixel 1 and 2 have less than 5% change from the

minimum point in the bias current range of (0.022mA to 0.030mA).

In order to improve the receiver noise temperature, an AR coating as described in the Chapter II is designed and manufactured. Since this coating will be applied for both 1.4 and 1.9THz HEB mixers in the STO2 project, we measure the noise temperature improvement for both frequencies. The 1.4THz mixer we use is the pixel 1 in Figure 38, and the physical dimension of the 1.9 THz mixer is summarized in the Table VII. The measurement scheme is traditional one pixel measurement which can be found in [25]. All the measurement conditions are the same as before except the lens, and the results are shown in the Figure 38.

The noise temperature improvement for 1.4 THz HEB mixer is about 33%, while the improvement for 1.9 THz is about 32%. The results indicate that the coating indeed works at both frequencies.

Table VII. Physical dimensions of 1.9THz HEB mixer

	Frequency (THz)	W bridge (um)	L bridge (um)	R_{rt} (Ohm)
MV14 C11	1.9	1.5	0.14	130

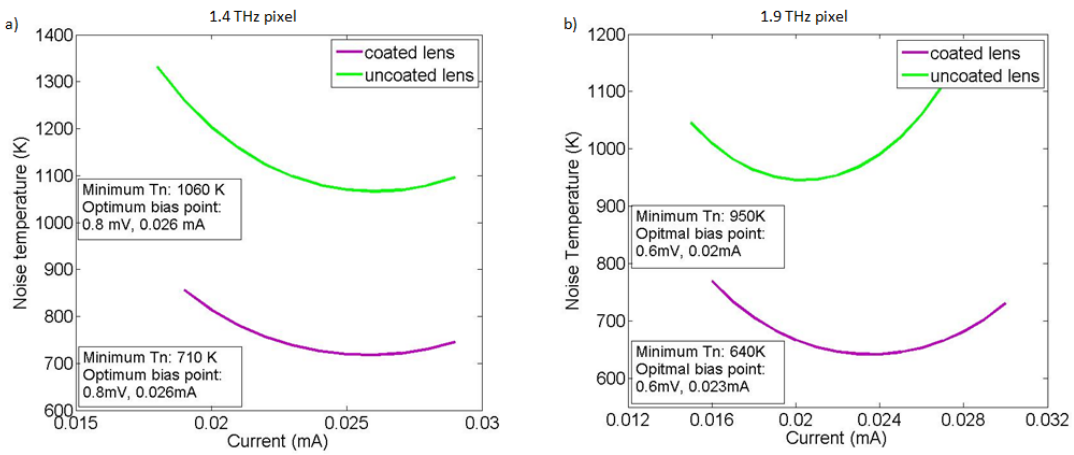

Figure 38. a: Receiver noise temperature measurement results for uncoated and coated lens at 1.4THz; b: Noise temperature results for 1.9 THz receiver.

7.3 IF Bandwidth Performance

The IF noise bandwidth of the 1.4 THz HEB mixer pixel 1 is also measured at the optimal bias point (0.8mV, 0.026mA). The measurement range is 0-7 GHz, and the result is shown in the Figure 39.

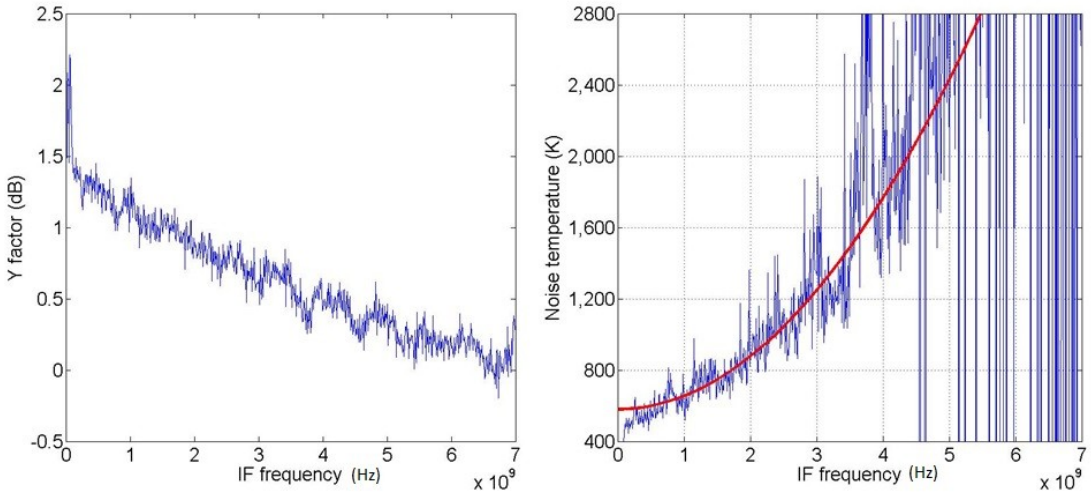

Figure 39. IF Y factor (left) and IF noise temperature bandwidth (right) of 1.4 THz pixel 1. The red curve in right figure is the fitting curve of the IF noise temperature, which is: $Tn = T_0(1 + \left(\frac{f}{fBW}\right)^2)$. T_0 is the noise temperature at zero IF frequency point and fBW is the fitting parameter.

The Y-factor result indicates that there is no significant standing wave problem in our IF chain. The IF noise temperature result gives the IF bandwidth by the fitting equation. For this mixer, the IF noise temperature bandwidth is about 3 GHz. And in an IF frequency range of 4 GHz, the noise temperature will be below 2000K.

7.4 Stability performance

7.4.1 Free running current

The instability of the HEB mixer limits the integration time of the receiver, and thus the detection performance. As pointed in the Chapter IV, there is an outstanding question whether the instability in the HEB current is dominated by the unstable LO power or the HEB mixer itself. Since we can measure the currents of the HEB array simultaneously and all sub LO beams are duplicated from the same source, it will be possible for us to answer this question.

Figure 40 is the measured currents of two pixels in time domain without applying any stabilization technique (free running state). The HEB mixers are all biased at 0.8mV, and the bias currents are set close to the optimal value (0.025mA) by reducing the incident LO beam power. The sampling rate is 1kHz and we average over 100 samples per point. Thus, the time between every two data point is actually 0.1s. The whole measurement takes about 4min.

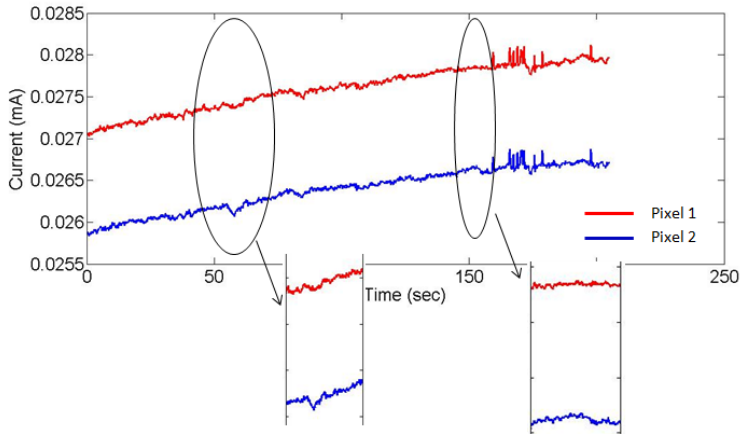

Figure 40. Measured currents of two free running pixels in time domain.

Two currents in the Figure 40 are found highly correlated with each other, which indicates that the instability in these two currents should come from the same source, that is the LO beam. Some details, however, are not so correlated if we zoom in. This can be explained by the different current responses (dP/dI) of different HEB mixers. This implies that the sensitivity to the same LO power change is slightly different for these two mixers. We can further prove this by comparing two currents in the frequency domain. Another possible reason is that the two sub LO beam coupled power is not changing exactly the same, due to the different standing waves in LO-mixer path, different air absorption and different mechanical vibrations on the beam splitter. The first two might be caused by the different optical path length from the grating to the mixer for different sub LO beams. A better alignment scheme will be helpful.

To analyze current in the frequency domain, the sampling frequency should be twice of the signal frequency in order to recover the original signal, according to the Nyquist sampling theory. We sample the signal with 1kHz frequency, and sample 20000 data points. Then the FFT transform is applied to obtain the signal in frequency domain. The normalized results for two pixels are shown in the Figure 41.

In the frequency domain, the two currents have exactly the same frequency features. Since the LO noise is mainly low frequency component, we zoom in on the frequency region from 0 to 20Hz. The same frequency features indicate that the noises in these two currents are generated by the same noise source. The only common things between these two currents are the sub LO beams, which are duplicated from one original beam. Thus, we could prove that the unstable LO beam power is the dominator in the instability of the current. Moreover, the amplitudes of the two frequency features are not exactly the same, which indicate that the same frequency components have different influence on each device. This is due to the different dP/dI of the two HEB mixers.

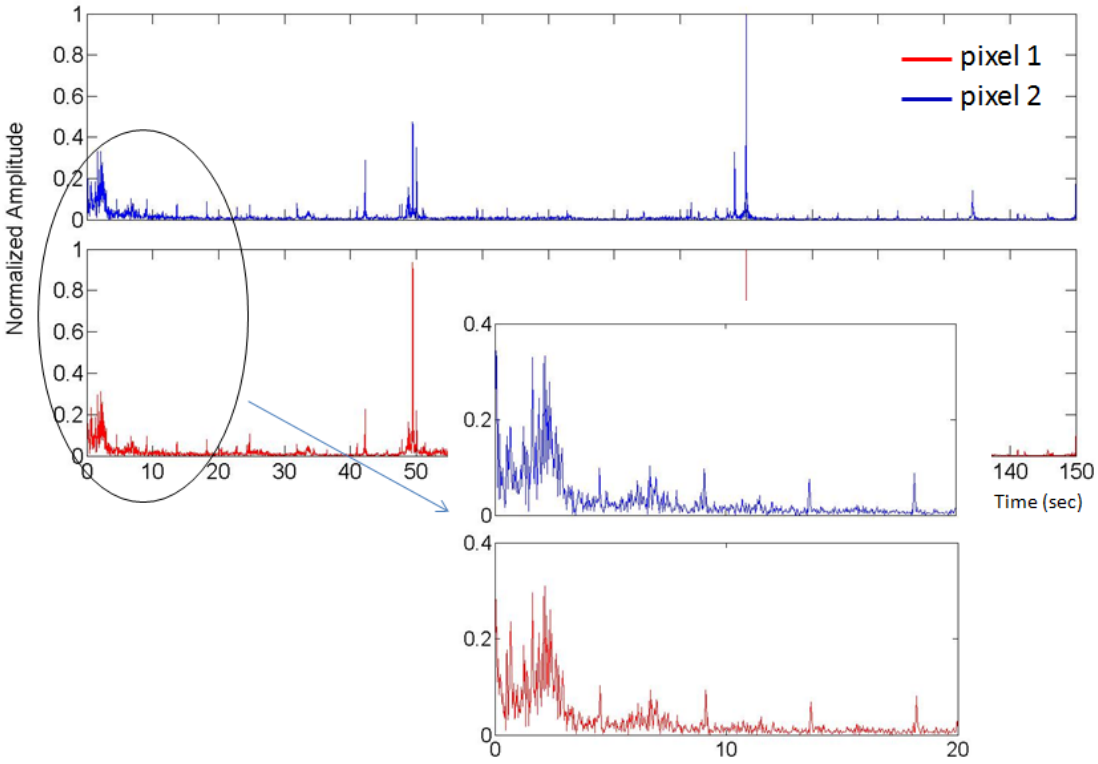

Figure 41. Measured currents of two free running pixels in frequency domain.

7.4.2 Stabilize two currents using one PID controller

Since the sub LO beams are all duplicated from one original beam, and two currents are highly correlated with each other, there is a possibility that we could stabilize two currents by using one PID controller. As described in the Chapter IV and Figure 27, the idea is to stabilize one pixel by applying the voice coil on the original LO beam, and hopefully the second pixel will also be stabilized. The measurement result is shown in the Figure 42. The sampling rate, averaging data number and measurement time are the same as the previous free running measurement.

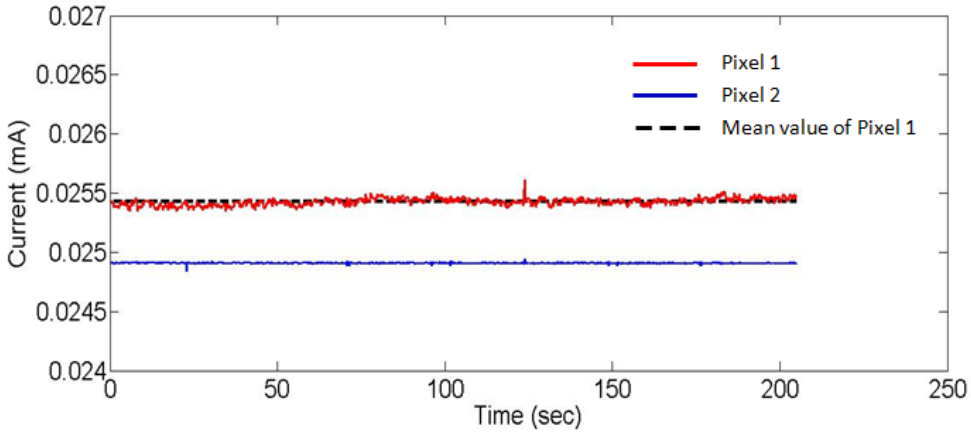

Figure 42. Measured currents of one stabilized pixel (pixerl2) and one free running one (pixel1).

Comparing with the two currents in Figure 40, we can find that the voice coil indeed

stabilizes two currents simultaneously. Although the current of pixel 1 is still quite noisy comparing to the current of pixel 2, the drift in two currents are successfully controlled, which is the most significant factor limiting the receiver Allan variance time.

In order to further prove the improvement of the receiver stability using this stabilization method, we also compare the Allan variance time of the two pixels simultaneously with and without applying voice coil. Before this, we firstly characterize the Allan variance time of the IF chain by setting the HEB mixer in superconducting state. The result is shown in the Figure 43.

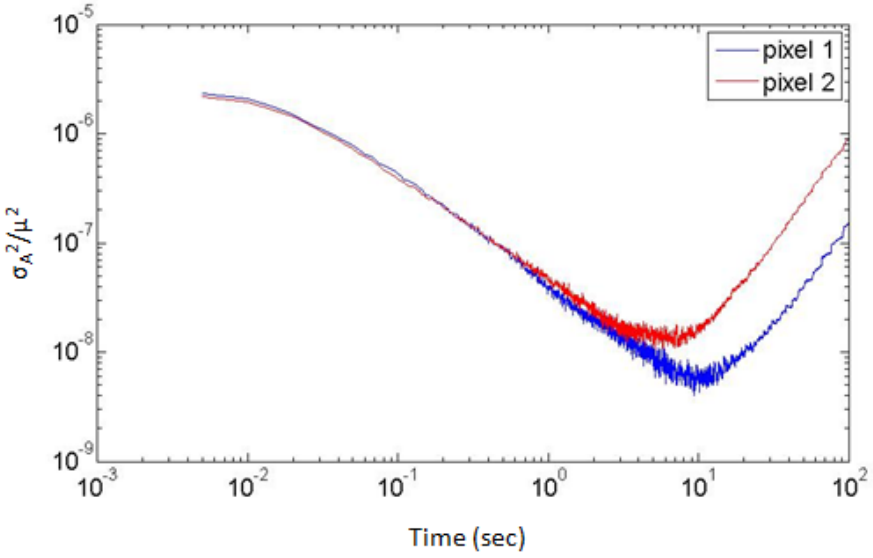

Figure 43. Allan variance time for two IF chains when the HEB mixers are in superconducting states. The Allan variance is normalized to the square of the raw data mean value. The Allan variance time for the two IF chains are about 10sec.

The two IF chains have an Allan variance time about 10sec, while the IF chain of pixel 1 is slightly better than that of pixel 2. The Allan variance time of the IF chain also gives the up limit for the receiver stability. Whatever the stability of the HEB mixer is, the stability of the whole receiver can never be better than the stability of the IF chain. Figure 44 shows the stability comparison of free running group and stabilization group. Both groups are bias at optimal bias points.

For non stabilization results, the two channels have a similar Allan variance time of about 0.15s. The drift noise dominates the noise spectrum after the white noise, and it seriously limits the stability performance. When the stabilization is applied on one pixel, the Allan variance time for the free running pixel (pixel 1) is about 0.8s, while for the stabilized one, the time is about 1.5s. The stability of the two pixels are improved by a factor of about 8 and 10 respectively. In the stabilized results, both pixels have a significantly reduced drift noise comparing to the free running results, which proves that the stabilization indeed works on both pixels.

However, the stability of the free running pixel in stabilization group is dominated by the 1/f noise after the white noise part, while the 1/f noise is not so significant in stabilized one. The strong 1/f noise indicates that the noise source in free running pixel of stabilization group is mainly from the electronic device. This can be explained by the poor noise performance of the bias supply we use. The current we used to implement stabilization is the read out current from the

bias supply I_{mon}. This current is the real current of the HEB mixer I_{real} together with the noise from the electronic components in the bias supply. For the stabilized pixel, this noise is eliminated by changing the incident LO power. But for the free running pixel in stabilization group, the bias supply has its independent electronic noise, so the electronic noise in the stabilized pixel will be added to its own electronic noise through the change of the LO power. Thus, the 1/f noise becomes significant in this pixel.

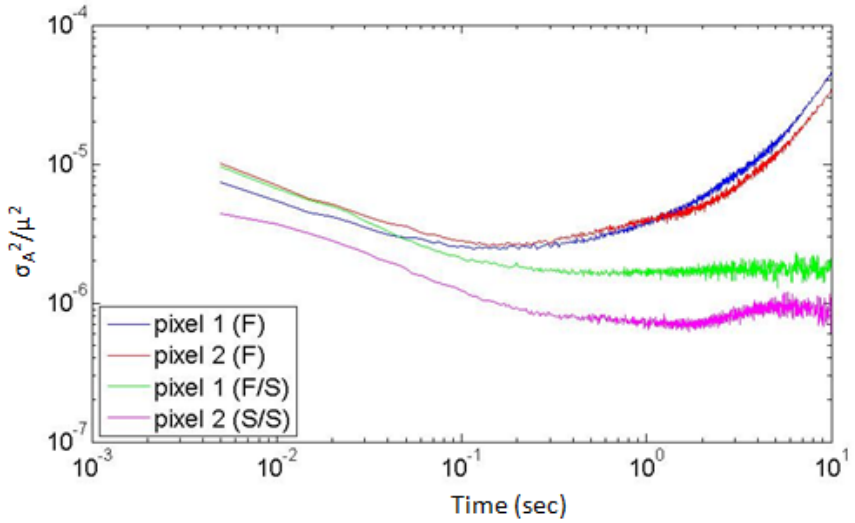

Figure 44. Allan variance time for two IF chains when the HEB mixers are in optimal pumped states. The Allan variance is normalized to the square of the raw data mean value. The Allan variance time for the free running two pixels (blue and red) is about 0.15s. The Allan variance time for free running pixel in stabilization group (green curve) is about 0.8s, while for stabilized pixel (purple curve) is about 1.5s

VIII

Summary and Outlook

This report elaborates my thesis project on building a 1.4 THz 2×2 heterodyne receiver array based on a Fourier phase grating. Here is the summary of the main work:

1. We review the previous terahertz receiver array applications and suggest our array configurations and LO multiplexing technique, which are based on HEB mixers and a Fourier phase grating. To the authors best knowledge, our array is the first quasi-optic HEB mixer array which can work at above 1 THz based on Fourier phase grating.

2. We measure the beam patterns of the 1.4 THz phase grating, and compare the measurement results with the theoretical one. The LO optical path for the 1.4 THz HEB mixer array is also designed and verified. The original LO beam can be uniformly split into a 2×2 array with a spacing of 12mm between each sub LO beam, which fits the mixer block.

3. The efficiency of the phase grating at 1.4 THz is also determined. The result indicates that the grating has an efficiency around 70%, which is very promising.

4. We prove that all pixels in the receiver array can be fully pumped by each sub LO beam when we apply an FIR gas laser at 1.4 THz as the incoming source. And we also indicate that by reducing the LO power level, all the pixels can be optimally pumped by each sub LO beam. simultaneously. The required LO power to optimally pump each pixel is similar at around 160nW. By assuming the beam splitter has a reflection efficiency of 10%, the total required incoming LO power for optimally pump is ~25μW.

5. We measure the noise temperature of two pixels with uncoated lenses in our receiver array, and find their optimal pumped region. In order to improve the receiver noise temperature, we also apply an AR coating on the lens. We compare the receiver noise temperature with coated and uncoated lens, and prove the AR coating indeed help improve the receiver performance by about 30%.

6. We analyze the currents of two HEB mixers in time and frequency domain. The high correlation between two currents in the time domain and the same frequency features of two currents in frequency domain prove that the unstable LO power is the dominator in current instability.

7. Based on this high correlation between currents, we come up with a new stabilization method for the array which only needs one PID controller. We compare the Allan variance time of two pixels with and without applying this new stabilization method, and prove this method can improve the Allan variance time of two pixels significantly.

This thesis project successfully builds a 1.4 THz heterodyne receiver array which can be stabilized using only one set of stabilization device. And it can serve as a prototype for future 4.7THz heterodyne receiver in the GUSSTO project. The performance of this array, like the noise temperature, IF bandwidth and Allan variance time are characterized. This thesis work can be further improved by:

1. Make a better and easier optical alignment scheme since sub LO beams may suffer from different distortions and losses when the optical alignment is not good. We should also use parabolic mirror instead of the lens to reduce the losses in the optical path.

2. Integrate the phase grating and other optical components in the cryostat, place the beam splitter in the vacuum. This allows us to measure in the vacuum environment, where the standing wave in LO-mixer path and air absorption can be eliminated.

3. Design new low noise bias supply, which can reduce the 1/f noise in free running pixel in stabilization group.

4. Polarizer might also be good candidate for stabilization, and they will not even change the LO beam shape. But the polarizer we have now is much less flexible than voice coil, and it can only control the current in a very small range. So a more flexible polarizer with large dynamic range should be designed and manufactured.

5. Minimize the IF circuits by using integrated circuit, which allows us to build a even larger array.

Appendix

A.1 Four wire measurement scheme

The measurement of the DC signal is measuring the bias voltage and current of the HEB. It is implemented by using a four-wire measurement technique since the resistance of the HEB is very small in low temperature environment. The four wire measurement is especially used for measuring low resistance component by ruling out the wire resistance influence in traditional two wire measurement. Figure 45a and b illustrate these two kinds of measurement circuit.

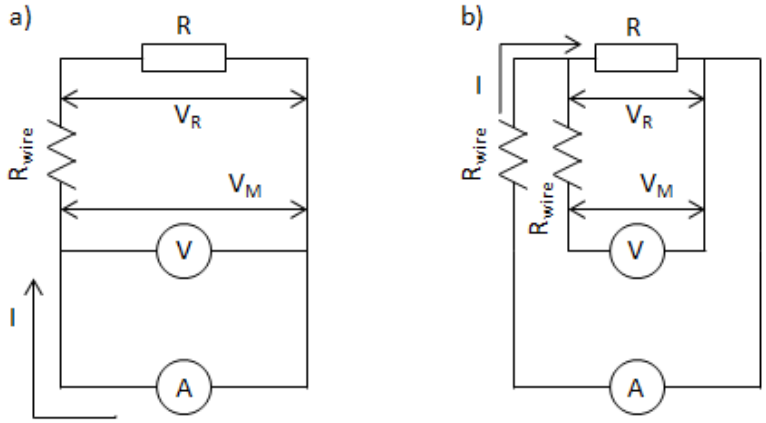

Figure 45. a: Two wire measurement circuit. b: Four wire measurement circuit

In traditional two wire measurement, the read out of the voltage meter is V_M, but the real voltage on the resistor we are going to measure is V_R. The difference is caused by the wire resistance:

$$\frac{V_M}{I} = R + R_{wire} \tag{60}$$

Since normally the wire has a resistance of 10mΩ to 1Ω, it is very difficult to get the accurate resistance value when the resistor under test is lower than 100Ω [38].

The four wire measurement, however, can measure the small resistance with a very high accuracy. The current is forced to flow through the resistor under test, instead of flowing through the voltage meter branch (R_{wire}) due to the large resistance of the voltage meter. Although some very small current might flow through the voltage meter branch, it has negligible influence on the measurement. So there is:

$$V_R \approx V_M$$
$$R = V_M/I \tag{61}$$

A.2 Safe Switch Circuit

Since the HEB mixer is a very delicate device, it is necessary to protect it from unwanted current when we are not measuring it. A safe switch circuit is applied to protect it, as depicted in the Figure 46.

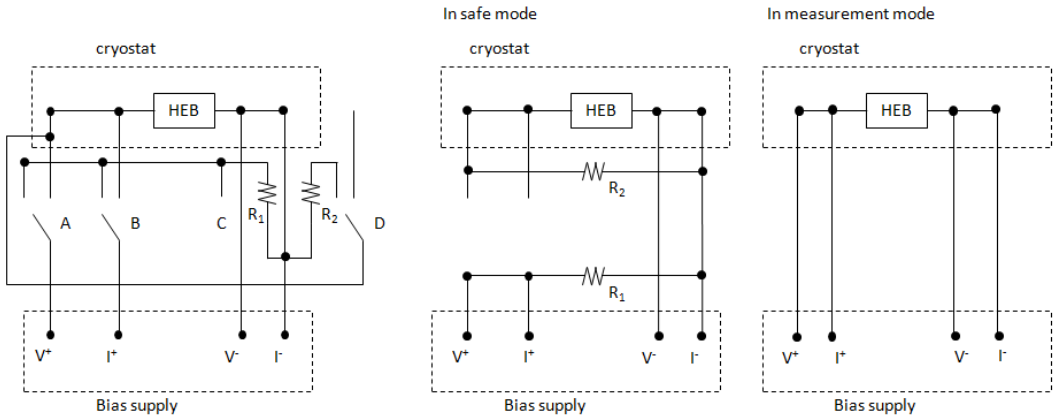

Figure 46. Safe switch of the HEB mixer. The A, B, C and D are four parallel single-pole double-throw switches which work simultaneously. R1 is a 22Ω resistor. R2 is a 1kΩ resistor, which is used to protect the HEB mixer.

When the switch is in the measurement mode, the HEB mixer is connected with the bias supply through four wires, V^+, V^-, I^+, I^-, as a standard four wire measurement circuit. When the switch is in the safe mode, the HEB mixer is disconnect with the bias supply and connected with a 1kΩ resistor, instead of being fully open circuit. This to protect the HEB mixer from being damaged from unwanted current.

A.3 Publication

26TH INTERNATIONAL SYMPOSIUM ON SPACE TERAHERTZ TECHNOLOGY, CAMBRIDGE, MA, 16-18 MARCH, 2015

A 2 × 2 Array Receiver at 1.4 THz based on HEB mixers and a Fourier Phase Grating Local Oscillator

X.X. Liu[1,2], D. J. Hayton*[1], Y.C. Luo[3], L. Wei[4], N. Vercruyssen[3] J.R. Gao[1,3], and C. Groppi[5]

[1] *SRON Netherlands Institute for Space Research, Groningen/Utrecht, the Netherlands*

[2] *Microelectronics Department, Delft University of Technology, Delft, the Netherlands*

[3] *Kavli Institute of NanoScience, Delft University of Technology, Delft, the Netherlands*

[4] *Imaging Physics Department, Delft University of Technology, Delft, the Netherlands*

[5] *School of Earth and Space Exploration, Arizona State University, AZ, USA*

*Contact: D.J.Hayton@sron.nl (or X.Liu-6@student.tudelft.nl), phone +31-50-3639363

Abstract— **We report on realization of a 2 × 2 NbN hot electron bolometer (HEB) array receiver using multiple local oscillator (LO) beams that are obtained from a Fourier phase grating mirror. The grating splits a 1.4 THz single beam into four uniform sub-beams. Two 50mm lenses are applied to collimate each beam in order to achieve a spacing of 12mm between them. The LO power in each beam is shown to be enough to fully pump the HEB mixer elements. The IV curves, noise temperature and IF bandwidth for each pixel is then characterized.**

Introduction

For heterodyne radio astronomy receivers above 1 THz, the superconducting NbN HEB is the most suitable mixing detector due to its operating frequency range, near quantum noise limit performance, low local oscillator (LO) power consumption, and no needs for an external magnetic field. They have been used in several astronomic telescopes[1,2,3] for mapping fine structure lines. One of the structure lines is the ionized nitrogen line [NII] at 1.4 THz.

The mapping process, however, is inefficient for a single pixel receiver. Thus, an HEB array receiver is preferred to improve the mapping speed while retaining excellent performance. A number of studies[4,5] have demonstrated HEB arrays and characterized their performance. Despite the difference in array structure, all of these arrays use a divergent LO beam to pump the HEB mixers. A large percentage of LO power will be wasted in this way. In addition, each pixel may suffer from a non-uniform distribution of the LO power.

Based on the Fourier series expansion theory, a grating mirror that can transform a single 1.4 THz LO beam with an incident angle of 25 deg into a 2 × 2 pattern of four LO beams is designed[6]. We applied two identical lenses to achieve collimated far field beams at a spacing of 12mm between each beam, which is consistent with the HEB elements in our array mixer block (Fig 1b). Each pixel is then biased independently and has its own IF chain. The IV curve, LO power budget, noise temperature and IF bandwidth are determined for each pixel. Since only two ports are available in our measurement cryostat at the moment, we characterize our array in pairs of pixels, keeping one pixel as the reference and measure other three.

Measurement Scheme

The HEB mixer array block and measurement setup for our array receiver are shown in Fig 1.

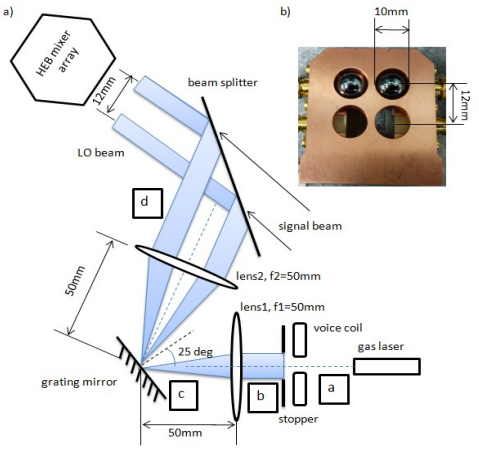

Fig 1. a) Optical part of the measurement setup. b) Layout of the block of four HEB mixers.

Our 1.4 THz LO is originated by an Far-Infrared gas laser with approximately 1mW emitted power. The LO power is stabilized using a voice coil based on optical attenuator that uses the HEB bias current to remove amplitude fluctuations in the laser[7]. A variable aperture stop is used to control the beam size in order to avoid overlapping between each beam. It also helps to achieve a Gaussian beam by blocking the ring around the main beam. The grating mirror is placed at the focal point of two 50mm High Density Polyethylene (HDPE) lenses to achieve a desired peak-to-peak spacing between beams, and to collimate each beam.

Finally, the 4 beams are reflected from a 6 μm thick beam splitter so that they can be combined with a hot/cold load for characterization of the mixer sensitivity. The IF circuit of each pixel, LO budget calculation, noise temperature and IF bandwidth measurement techniques can be found elsewhere[8,9].

RESULTS

A. 2 × 2 LO Beam Patterns

Fig 2 shows the beam pattern along the optical path (see Fig 1a). The beam patterns after lens2 indicate four, nearly collimated Gaussian beams. The peak to peak spacing is around 12mm, while the diameter of each beam is about 7mm. This pattern is perfectly matched to our array block in Fig 1b).

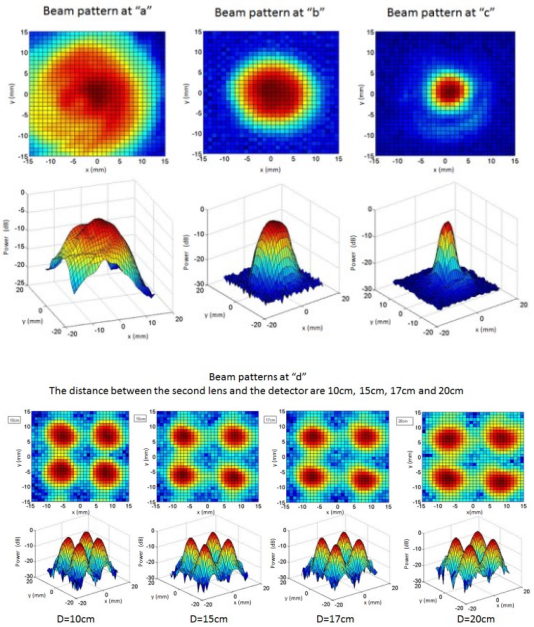

Fig 2. LO beam patterns along the optical path

B. IV Curves of Two Pixels Array

For the first time, we tried to pump a 1 x 2 mixer array due to the limitation of our cryostat window. Fig 1 b) is the layout of our array and each element is a twin slot antenna coupled NbN HEB mixer with the same HEB dimensions, as shown in the Table 1.

TABLE 1

DIMENSIONS OF THE HEB MIXERS AND THE TWIN SLOT ANTENNA

HEB mixer				
l (um)	w(um)	t (nm)	R (Ohm)	Tc (K)
0.19	1.5	7	130	9.45
Twin slot antenna				
L (um)	W (um)	S (um)	Frequency (THz)	
61	5	35	1.4	

Note: l and w are the length and width of the bolometer, t is the NbN thickness, R is the resistance in room temperature and Tc is the critical temperature. L, W and S are the length, width and separation of the twin slots. Frequency is the designed operational frequency for the twin slot antenna.

The IV curves of the pumped HEB mixer array are plotted in the Fig 3. We move the cryostat 12mm vertically and two mixers array is again fully pumped by the other two beams. This indicates that if we have four pixels, all of them would be fully pumped.

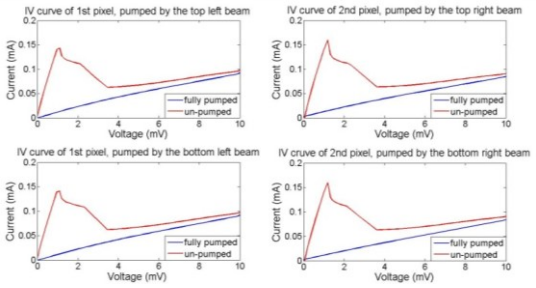

Fig 3. IV curves two HEB mixers: un-pumped and pumped state. The top two IV curves are pumped by the top two LO beams, while the bottom two are pumped by the bottom two LO beams.

C. Bias Currents of Two Pixels

The two bias currents of the HEB mixer array are measured simultaneously under fully pumped and optimal pumped (0.8mV, 0.028mA) situation without any stabilization, as shown in the Fig 4. The current scale is set to be the same in order to compare the fluctuations in currents under two pumping cases.

The Pearson product-moment correlation coefficient is defined as the measurement of linear dependence of two variables. The correlation coefficient between currents of two pixels in fully pumped case is 0.15, while the correlation coefficient in the optimally pumped

case is 0.8, that indicates a very strong correlation between the two pixels' currents in this case. The very week correlation between the currents in fully pumped situation is because the two HEB mixers are already saturated. So the fluctuation in LO power has no significant influence on the current stability. The strong correlation in optimal pumped situation is due to the fact that two LO beams are duplicated from the same LO beam. This also suggests that the instability in current of the HEB mixer is mainly caused by the fluctuation in LO power.

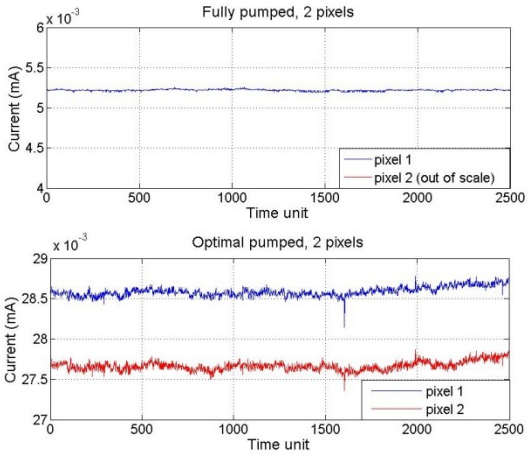

Fig 4. Currents of two HEB mixers under fully pumped and optimal pumped situations.

D. Expected Results

This measurement is being expanded to characterize all four mixers. Data will be presented for noise temperature and IF bandwidth of the full array. Moreover, the possibility of using one voice coil to stabilize the bias current of four HEB mixers will be investigated.

CONCLUSIONS

We succeed in applying a designed Fourier phase grating mirror in our HEB array receiver at 1.4 THz. We demonstrate that our phase mirror provides an efficient and highly uniform distribution of the LO power that was not previously possible with the flood illumination approach. A beam pattern well matched to our array is formed using 2 lenses in combination with the Fourier phase grating. A 2 × 2 array is then fully pumped for the first time. Based on the correlation of two pixels' currents, we prove that the fluctuation in LO power is the main contributor to the instability of the bias currents.

Acknowledgement: We thank Chris Walker for many valuable discussions on the array.

REFERENCES

[1] Güsten, Rolf, et al. "GREAT: the first-generation German heterodyne receiver for SOFIA." Proc. SPIE. Vol. 4014. (2000).

[2] S. Cherednichenko et al. "Hot-electron bolometer terahertz mixers for the Herschel Space Observatory." Review of scientific instruments 79.3 (2008): 034501.

[3] C. Walker et al. "The Stratospheric THz Observatory (STO)." SPIE Astronomical Telescopes+ Instrumentation. International Society for Optics and Photonics, (2010).

[4] F. Rodriguez-Morales et al. "A terahertz focal plane array using HEB superconducting mixers and MMIC IF amplifiers." Microwave and Wireless Components Letters, IEEE 15.4 (2005): 199-201.

[5] L. Liu et al. "Integrated 585-GHz Hot-Electron Mixer Focal-Plane Arrays Based on Annular Slot Antennas for Imaging Applications." Microwave Theory and Techniques, IEEE Transactions on 58.7 (2010): 1943-1951.

[6] Y.C. Luo et al, “Fourier phase grating for THz multi-beam local oscillators”, Extensive abstract to ISSTT 2015 (same conference) .

[7] D. J. Hayton et al. "Stabilized hot electron bolometer heterodyne receiver at 2.5 THz." Applied Physics Letters 100.8 (2012): 081102.

[8] D. J. Hayton et al, A 4.7 THz Heterodyne Receiver for a Balloon Borne Telescope, Proceedings of SPIE, Millimeter, Submillimeter, and Far-Infrared Detectors and Instrumentation for Astronomy VII, 24-27 June, 2014, Montreal, Canada, Editors by Wayne S. Holland, and Jonas Zmuidzinas, pages 91531R 1-7

[9] J. L. Kloosterman et al; Hot electron bolometer heterodyne receiver with a 4.7-THz quantum cascade laser as a local oscillator, Appl. Phys. Lett. 102, 011123 (2013).

Acknowledgement

Firstly, I would like to appreciate my SRON supervisor Dr. Darren Hayton, who is also one of my best friends. Thanks to his instructions and guidance, lots of difficulties and challenges in this thesis work can be solved perfectly. Besides the academic knowledge, I also learned a lot from his personality and attitude towards the work and life. His great devotion to the job and passion in discovering the world will always inspire me in my future life.

Secondly, I would like to thank Dr. Jianrong Gao, who provides this thesis opportunity to me in SRON. He helps me a lot in understanding the physical knowledge of the HEB mixer, and the theoretical reasons behind the measurement results. His hardworking attitude and fully devotion to the scientific world also encourages me a lot.

I also would like to appreciate the help from my TU Delft supervisor assistant professor Dr. Akira Endo. Although most of this thesis work is done in SRON, he is always willing to give me his best help when I have trouble in my work. He provides me with many precious suggestions after my mid-term report. These suggestions correct some misunderstandings of mine in theoretical knowledge of the measurement.

Moreover, I would like to thank professor Dr. Andrea Neto in TU Delft. I had three lectures given by Professor Neto in the first year of my master study, all of them are relating to the electromagnetic waves, antennas and terahertz technology. His great lectures open the door for me to investigate this wonderful terahertz world. Prof. Neto also supports me a lot in performing this master thesis in SRON.

In addition, I would like to appreciate my nice SRON colleagues and friends. Leo de Jong helps me with the wire bonding work. He has been worked in SRON for more than 50 years. His perfect wire bonding skill is of great importance to the realization of the array. Willem Jan, a nice scientist in SRON, helps me a lot in selecting optical lenses and using gas laser. He also teaches me how to make traditional Dutch pudding, which is really delicious. Detrain Axel and Smit Heino help me a lot in electric circuit part of the cryostat. Andrey Khudchenko gives me lots of suggestions on the HEB stability issues. Ferrari Lorenza lends me her current amplifier. Wouter Laauwen helps me with the optic alignment work, and Duc helps to put the absorbing material on the mixer block, etc.

This is my first time to "work" in such an international environment. And all of my colleagues are willing to help me not only in academic world, but also in daily life. Their help makes me feel like at home.

I also would like to thank my parents and friends in TU Delft. They encourage me a lot in this master study process and the life in the Netherlands.

Last but not the least, I appreciate the TU Delft who provides me with a scholarship that enables my study and stay in Netherlands. Without this I could not enjoy such a wonderful two years journey here.

Reference

[1] Kulesa, Craig. *Terahertz spectroscopy for astronomy: From comets to cosmology.* Terahertz Science and Technology, IEEE Transactions on 1.1 (2011): 232-240.

[2] Reese, Matthew Owen. *Superconducting hot electron bolometers for terahertz sensing*. Diss. Yale University, 2006.

[3] Irwin, Kent D., and Gene C. Hilton. *Transition-edge sensors*. Cryogenic particle detection. Springer Berlin Heidelberg, 2005. 63-150.

[4] Irwin, K. D. *An application of electrothermal feedback for high resolution cryogenic particle detection*. Applied Physics Letters 66.15 (1995): 1998-2000.

[5] Mazin, Benjamin A. *Microwave kinetic inductance detectors*. Diss. California Institute of Technology, 2004.

[6] Sizov, F., and A. Rogalski. *THz detectors*. Progress in Quantum Electronics 34.5 (2010): 278-347.

[7] Kooi, Jacob Willem. *Advanced receivers for submillimeter and far infrared astronomy*. Rijkuniversiteit Groningen, 2008.

[8] Zmuidzinas, Jonas, Alexandre Karpov, and David Miller. *Coherent detection and SIS mixers.* Proceedings of the Far-IR, Sub-MM, and MM Detector Technology Workshop, Monterey, California. 2002.

[9] Chattopadhyay, Goutam, et al. *Development of multi-pixel heterodyne array instruments at submillimeter wavelengths*. Invited Paper–in Proceedings of the Asia Pacific Microwave Conference. 2004.

[10] Rabanus, David, et al. *Techniques for Heterodyne Array Receivers*. Proc. Far-IR, Sub-MM, and MM Detector Technology Workshop. Montery, CA, 2002.

[11] Groppi, C., et al. *Heterodyne Array Development at the University of Arizona*. Proc. 14th. Intl. Symp. Space THz Tech. 2003.

[12] Graf, Urs U., et al. *SMART: The KOSMA sub-millimeter array receiver for two frequencies.* Astronomical Telescopes and Instrumentation. International Society for Optics and Photonics, 2003.

[13] Schuster, Karl-Friedrich, et al. *The IRAM 230-GHz multibeam SIS receiver*. Astronomical Telescopes and Instrumentation. International Society for Optics and Photonics, 2000.

[14] Kasemann, C., et al. *CHAMP+: A powerful submm Heterodyne Array*. 19th International Symposium on Space Terahertz Technology. 2008.

[15] Walker, C. K., et al. *The Stratospheric Terahertz Observatory (STO)*. Proceedings of the 19th ISSTT, Groningen (2008): 28-32.

[16] Risacher, Christophe, et al. *The upGREAT heterodyne array receivers for far Infrared astronomy*. Infrared, Millimeter, and Terahertz waves (IRMMW-THz), 2014 39th International Conference on. IEEE, 2014.

[17] Rodriguez-Morales, Fernando, et al. *A terahertz focal plane array using HEB superconducting mixers and MMIC IF amplifiers.* Microwave and Wireless Components Letters, IEEE 15.4 (2005): 199-201.

[18] Rieke, George. *Detection of Light: from the Ultraviolet to the Submillimeter*. Cambridge University Press, 2003.

[19] Floet, D. Wilms, et al. *Hotspot mixing: A framework for heterodyne mixing in superconducting hot-electron bolometers.* Applied physics letters 74.3 (1999): 433-435.

[20] Merkel, Harald, et al. *A hot-spot mixer model for phonon-cooled NbN hot electron bolometric mixers*. Applied Superconductivity, IEEE Transactions on 9.2 (1999): 4201-4204.

[21] Rodriguez-Morales, Fernando, K. Sigfrid Yngvesson, and Dazhen Gu. *Wideband IF-integrated terahertz HEB mixers: Modeling and characterization.* Microwave Theory and Techniques, IEEE Transactions on 58.5 (2010): 1140-1150.

[22] Semenov, Alexei, et al. *Intermediate Frequency Bandwidth of a Hot-Electron Mixer:*

Comparison with Bolometric Models. Seventeenth International Symposium on Space Terahertz Technology, held May 2006 at Observatoire de Paris, LERMA. Paris, France., p. 72. Vol. 1. 2006.
[23] Filipovic, Daniel F., Steven S. Gearhart, and Gabriel M. Rebeiz. *Double-slot antennas on extended hemispherical and elliptical silicon dielectric lenses.* Microwave Theory and Techniques, IEEE Transactions on 41.10 (1993): 1738-1749.
[24] Dou, W. B., and Z. L. Sun. *Ray tracing on extended hemispherical and elliptical silicon dielectric lenses*. International journal of infrared and millimeter waves 16.11 (1995): 1993-2002.
[25] Hajenius, M., et al. *Full characterization and analysis of a terahertz heterodyne receiver based on a NbN hot electron bolometer.* Journal of applied physics 100.7 (2006): 074507-074507.
[26] Vorst M J M. *Integrated lens antennas for submillimetre-wave applications*[D]. Technische Universiteit Eindhoven, 1999.
[27] Born, Max, and Emil Wolf. *Principles of optics: electromagnetic theory of propagation, interference and diffraction of light*. Cambridge university press, 1999.
[28] Graf, Urs U., and Stefan Heyminck. *Fourier gratings as submillimeter beam splitters.* Antennas and Propagation, IEEE Transactions on 49.4 (2001): 542-546.
[29] Yuchen. *Demonstrating a Fourier phase grating for a terahertz multi-beam local oscillator.* Delft University of Technology, 2014.
[30] Kerr, Anthony R., Marc J. Feldman, and Shing-Kuo Pan. *Receiver noise temperature, the quantum noise limit, and the role of the zero-point fluctuations*. Proc. Eighth In tern. Space THz Technol. Symp. 1997.
[31] Jochem Baselmans. *HEB Project in Groningen: Practical notes.* 2003
[32] Kooi, J. W., et al. *Stability of heterodyne terahertz receivers.* Journal of applied physics 100.6 (2006): 064904.
[33] Allan, David W. *Statistics of atomic frequency standards.* Proceedings of the IEEE 54.2 (1966): 221-230.
[34] Schieder, R., and C. Kramer. *Optimization of heterodyne observations using Allan variance measurements.* Astronomy & Astrophysics 373.2 (2001): 746-756.
[35] Tobias Markl, *1/f Noise, Telegraph Noise.* Slides from Physikalischen Instituts of Karlsruhe Institute of Technology, 2009.
doi:http://www.phi.kit.edu/noise/abbildungen/Noise-03_Non-Thermal_Noise_1_over_f_Noise.pdf
[36] D. J. Hayton et al. *Stabilized hot electron bolometer heterodyne receiver at 2.5 THz*. Applied Physics Letters 100.8 (2012): 081102.
[37] Khosropanah, P., et al. *Low noise NbN hot electron bolometer mixer at 4.3 THz*. Applied Physics Letters 91.22 (2007): 221111-221111
[38] KEITHLEY, *Overview of Two-Wire and Four-Wire (Kelvin) Resistance Measurements*, Application Note Series, Number 3176.